Alfred Wegener Institut
Technische Universität Berlin

Master thesis "Technischer Umweltschutz"

Characteristics and physical properties of Arctic aerosols

Fieke Rader

Matriculation number: 397290

1. Reviewer	Prof. Dr. Andreas Held Environmental Chemistry and Air Research Technische Universität Berlin
2. Reviewer	Dr. Christoph Ritter Atmospheric Physics Alfred Wegener Institut, Potsdam

October 2nd, 2020

Fieke Rader

Characteristics and physical properties of Arctic aerosols

Master thesis "Technischer Umweltschutz", October 2nd, 2020

Reviewers: Prof. Dr. Andreas Held and Dr. Christoph Ritter

Technische Universität Berlin

Alfred Wegener Institut, Potsdam

Declaration

Hiermit erkläre ich, dass ich die vorliegende Arbeit selbstständig und eigenhändig sowie ohne unerlaubte fremde Hilfe und ausschließlich unter Verwendung der aufgeführten Quellen und Hilfsmittel angefertigt habe.

, October 2nd, 2020

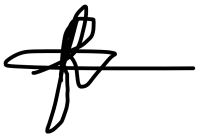

Fieke Rader

Abstract

In this master thesis, Raman Lidar data from Ny-Ålesund, Spitsbergen have been analysed for January to April 2019. Optical parameters (the aerosol backscatter at 532 nm, the depolarisation ratio at 532 nm, the color ratio and the Lidar ratio at 355 nm) and their typical values have been presented per height interval and per month, as well as the differences between those. Also, the links between the different optical parameters have been investigated and those values were compared with values of March 2018. March 2019 showed lower backscatter and higher depolarisation ratios, indicating fewer and more spherical particles as in March 2018. For January the 28^{th} and February the 06^{th}, hygroscopic growth has been determined. Relative humidity data measured by radiosondes have been investigated for strong gradients and backscatter data has been plotted against the relative humidity. The parametrization of the scattering enhancement factor ($f(RH) = (1 - RH)^{-\gamma}$) has been used to plot growth curves through the backscatter data and optimal values for γ have been found. For the 28th of January, the calculated γ-values ranged from 0.3 to 1.4 and the most likely value appeared to be 0.64. Growth factors ($g(RH)$) and γ-values have been calculated as well based on *in situ* (PM10-filter) data using the Zdanovskii-Stokes-Robinson relation. The resulting γ-values for January the 28th and February the 6th were respectively 0.98 and 0.73. For the 19th of January, a general overview of the aerosol situation on that day has been presented using different results from different techniques. Mostly small sized aerosol particles (14<D<300 nm) have been found for that day and low depolarisation values were measured, indicating the presence of small, spherical ammonium sulfate species. Further research combining Lidar and *in situ* data is needed for making more precise and accurate conclusions considering Arctic aerosols.

Zusammenfassung

In dieser Masterarbeit wurden Raman Lidardaten aus Ny-Ålesund, Spitsbergen von Januar bis April 2019 analysiert. Für unterschiedliche optische Parameter (die Aerosolrückstreuung bei 532 nm, das Depolarisationsverhältnis bei 532 nm, das Farbverhältnis und das Lidarverhältnis bei 355 nm) wurden deren typische Werte, Unterschiede und Zusammenhänge pro Höheintervall und pro Monat berechnet und visualisiert. Diese Werte wurden ebenfalls mit den beobachteten Werten in März 2018 verglichen. März 2019 zeigte niedrigere Rückstreuung und höhere Depolarisationsverhältnisse. Das deutet auf weniger und sphärischere Partikel im März 2019 als im März 2018. Für den 28. Januar und den 6. Februar 2019 wurde zusätzlich das hygroskopische Wachstum berechnet. Daten der relativen Feuchte, gemessen von Radiosonden, wurden auf starke Gradiente geprüft. Die Rückstreuung wurde anschließend gegen die relative Feuchte verglichen und Wachstumskurven wurden bestimmt. Die Wachstumskurven basieren auf die Parametrisierung des "streuungs-verstärkungs-Faktor" ($f(RH) = (1 - RH)^{-\gamma}$) und passen zu den Rückstreuungsdaten. Unterschiedliche optimale Werte für γ wurden berechnet. Für den 28. Januar lagen die γ-Werte zwischen 0.3 und 1.4, allerdings war 0.64 der wahrscheinlichste Wert. Wachstumsfaktoren ($g(RH)$) und γ-Werte wurden unter anderem auf Grundlagen von *in situ* (PM10-Filter) Daten mit der Zdanovskii-Stokes-Robinson Beziehung berechnet. Die γ-Werte für den 28. Januar und den 6. Februar waren 0.98 beziehungsweise 0.73. Für den 19. Januar wurde ein Überblick über die Aerosolsituation dieses Tages, basierend auf unterschiedlichen Ergebnissen aus unterschiedlichen Datenquellen, präsentiert. Meistens kleine Aerosolpartikel (14<D<300 nm) und niedrige Depolarisationsverhältnisse wurden für den Tag gefunden und deuten auf die Präsenz von kleinen, sphärischen Ammoniumsulfatpartikeln. Weitere Forschung im Bereich der Kombination von Lidar- und *in situ*-Daten für genauere Schlussfolgerungen bezüglich Arktischen Aerosols wird zukünftig gebraucht.

Contents

1 Introduction

1.1 Relevance

1.1.1 Arctic amplification

Since 1880, the Earth has on average become 0.8°C degrees warmer and 2/3 of this increase happened in the last two decades. The last five years (2015, 2016, 2017, 2018 and 2019) were the warmest years on record (NOAA, 2020). Arctic air temperatures are increasing too and continuing to increase twice as fast as the global temperature, an effect called Arctic amplification (Richter-Menge et al., 2019). In 2016, the average annual surface air temperature (SAT) over land north of 60° was the highest measured since the observational record beginning in 1900. From October 2017 to September 2018, the second highest SAT was observed. Arctic temperatures averaged over five years from 2014-2018 exceed all previous records. The SAT of 2016 was 2.0°C above the 1981-2010 average, representing a +3.5°C increase since 1900. The central Arctic winters (January-March) from 2016 and 2018 were +6°C above the 1981-2010 baseline (Richter-Menge et al., 2019).

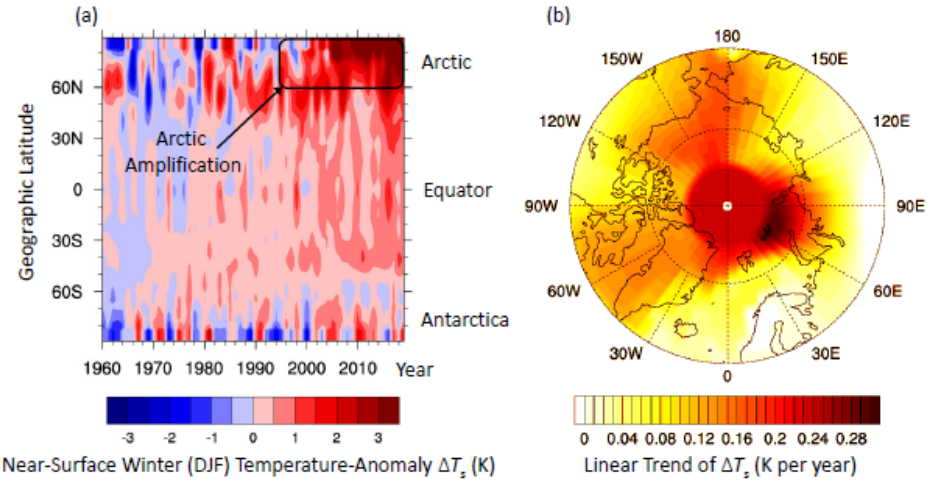

Fig. 1.1: 1 a) Trend of the annual-mean surface air temperature anomaly from 1990-2019 in units of Kelvin. The anomaly is calculated as the mean temperature between 1990-2019 minus the mean temperature between 1951-1980. Picture adopted from Wendish et al. (2017) by AC^3 ; b) Zonal annual mean temperature anomaly (K) per century compared to the 1990-2019 mean.

There are many factors, processes and peculiarities influencing the climate system in the Arctic. Unique features are the low solar elevation, the presence of polar days and nights, the large area of sea ice, the high surface albedo, a shallow atmospheric boundary layer and the presence of low-level mixed-phase clouds ((AC)^3, 2020). These factors are partly understood individually, however their interactions and collective influence on the Arctic climate are difficult to determine. The positive feedback mechanisms of ice and snow were for example long thought to be the driving factor behind the Arctic amplification, but models without snow and ice still show an amplifying effect in the Arctic. The exact mechanisms dominating Arctic amplification remain unclear, causing climate models to have difficulties in representing the Arctic climate (Wendisch et al., 2017).

1.1.2 Effect of aerosols on the Arctic climate

One of the factors influencing the Arctic climate are aerosols: suspensions of small solid particles or liquid droplets suspended in the air. Aerosols play an important role in the radiation budget of the Arctic and should be considered carefully in climate models. Their radiative effect can be divided in direct and indirect radiative effects. The direct radiative forcing of aerosols comes from their own properties of scattering and absorbing sunlight and causes an albedo effect in the atmosphere and after deposition also on the sea ice. The scattering and absorbing properties depend on the type and size of the aerosol and will be discussed in more detail in section 1.2.

The indirect radiative effect of aerosols is due to the cloud forming properties aerosols have. Clouds can either cool down or warm up the surface, by respectively reflecting shortwave sunlight or by emitting infrared (longwave) radiation. The formation of water droplets from pure water vapor, called homogeneous nucleation, happens at several hundred percent of oversaturation. This is rare and happens only spontaneously and randomly. However, aerosols functioning as cloud condensation nuclei (CCN) (or in some cases as ice nuclei, IN) can cause condensation at lower water saturation values, a process called heterogeneous nucleation (Wallace and Hobbs, 2006a). Since clouds have a strong radiative effect, aerosols indirectly play an important role in the radiation budget. The amount and the size of CCNs in a cloud moreover influence the strength of the radiative effects of the clouds (see figure 1.2).

More precisely, the amount of CCN in a cloud determines its brightness, called the Twomey effect (Twomey, 1974). Many CCN will cause the formation of many cloud droplets and thereby making the cloud brighter. Also, many small particles take more time to coalesce to raindrop size than larger particles, therefore decreasing the precipitation efficiency and increasing the cloud's lifetime, known as the Albrecht

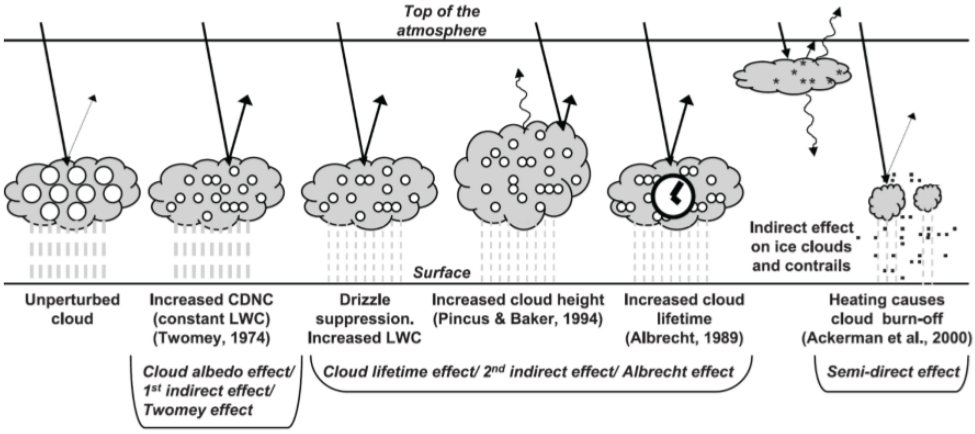

Fig. 1.2: Indirect radiative effects of aerosols Twomey, 1974

effect (Albrecht, 1989). The last indirect radiative effect actually is a semi-direct effect. Absorbing particles (such as black Carbon, BC) in clouds will warm up those clouds and contribute to their dissolution (Ackermann, 2000).

Depending on the type and size of aerosol, either warming or cooling can take place. Globally it is thought that the mass of aerosol particles has a stronger cooling than warming effect, but this effect differs locally. In the polar areas a rather warming effect by aerosols and its enhanced cloudiness is observed, mostly due to the high surface albedo and the low solar elevation, causing different reflection behaviour on aerosols and clouds (Lubin and Vogelmann, 2006). Large insecurities in the magnitude of the total anthropogenic CO_2 forcing exist in aerosol and cloud research (see figure 1.3). Generally, more research needs to be performed on aerosol and cloud research to decrease the insecurities and an additional focus on polar regions is needed due to their different (scattering) characteristics.

1.1.3 Arctic Haze and the effect of aerosols on the Arctic ecosystem

The effect of aerosols on the Arctic climate is particularly relevant during Arctic haze effects. Arctic haze is a phenomenon of relatively high turbidity in the Arctic, building up in wintertime and peaking in late winter/early spring. Vertical profiling and chemical fingerprinting of the haze showed the composition of the haze was a mixture of sulfates and particulate organic matter (POM), as well as ammonium, nitrates, dust, black carbon and some heavy metals (Quinn et al., 2002). Further research revealed the industrial, anthropogenic influence on the Arctic haze from the lower latitudes of the Eurasian continent (Shaw, 1983).

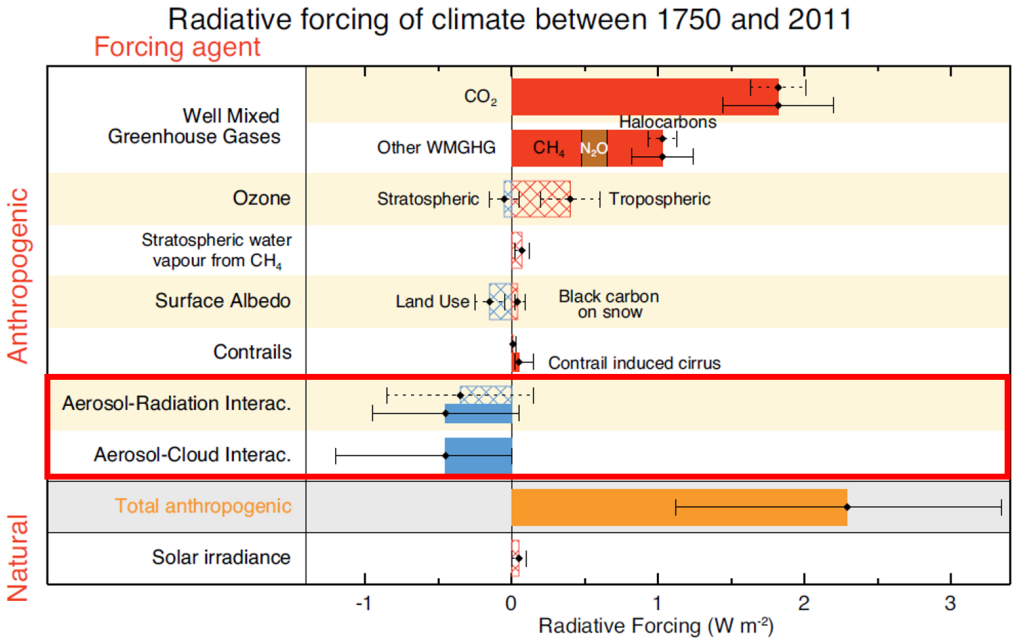

Fig. 1.3: Radiative forcing of climate between 1750 and 2011. The lines in the bars indicate the uncertainties from the 5 to 95% confidence range (Myhre et al., 2013).

During winter, strong temperature inversions cause a stably stratified troposphere and thereby obstruct turbulent vertical transport, cloud formation and precipitation. Like this, the major aerosol removal pathway is being inhibited and aerosols will become trapped and accumulate in the Arctic atmosphere. Additionally, the transport from the mid-latitudes towards the Arctic intensifies during winter and spring, causing an increased supply of aerosols from the lower latitudes.

Past Lidar data and aircraft measurements showed the Arctic haze occurs mostly in the lower 5 kilometer of the atmosphere, but peaking in the lower 2 kilometer and therefore has an impact on the environment on the soil and water too, including the organisms living there (Hoff et al., 1983),(Leaitch et al., 1989). Some of the aerosols and gases can be toxic, especially the heavy metals as well as persistent organics (e.g. PCB, pesticides). An illustrative example: breastfeeding women in local Arctic communities are advised to supplement the feed of the young baby with formula/powdered milk, due to possibly high concentrations of pollutions in the mother milk. When being released in the water, especially persistent organics are unlikely to be broken down and in the fatty tissue of larger sea animals, pollutions can accumulate and reach high concentrations. The consumption of those sea animals by the local Arctic populations will put them under health risks (and many larger arctic animals too) (EEA, 2017). Understanding the composition, the number and the mass of aerosols is therefore not only important from a climatological point of view (using the measurements to study aerosol mechanisms and optimizing climate models), but also from an ecological and toxicological one (Shaw, 1995). This master thesis

will contribute to the understanding of aerosol composition and mechanisms in the Arctic by analysing Lidar data from Spitsbergen, Ny-Ålesund. Before going into detail considering the study and the Lidar, more general information about aerosols will be given.

1.2 Introduction to aerosols and their physical and chemical properties

As stated before, aerosols are small particles or liquid droplets in the air. Their size ranges from approx. 1 nm to several tens of micrometers. Particles ranging from 1 nm to 1 μm are defined to be fine particles, whereas the ones ranging from 1 to 10 μm are called coarse particles. The small particles can be classified into three different stages. Very small particles ranging from 1 to 10 nm are said to be in the nucleation mode, particles from 10 to 100 nm in the Aitken mode and aerosols from 100 nm to 1 μm in the accumulation mode. Aerosols can have both natural and anthropogenic sources. Typical natural aerosols are sea salt, mineral dust and plant material, whereas typical anthropogenic sources of aerosols are traffic fumes, industrial processes and biomass burning (Boucher, 2015).

1.2.1 Formation and growth of aerosols

The *formation* of new aerosols can be distinguished in two pathways: the primary and the secondary formation. Primary particles are directly emitted into the atmosphere by processes such as biomass burning, volcanic eruptions or wind-driven suspension (like mineral dust or sea salt). The emission of biological aerosols such as pollen, viruses or bacteria are also considered primary aerosols. Secondary aerosols are being formed from the conversion of gases to particles and this involves the clustering of gas molecules (Boucher, 2015). However, most gas molecules have a too high vapor pressure (and are therefore too volatile), preventing nucleation. Therefore gases have to be oxidized in the atmosphere (lowering their vapor pressure) before nucleating. An example is the oxidation of sulfur dioxide (SO_2) into sulfuric acid (H_2SO_4). H_2SO_4, having a low vapor pressure, can then condensate with water or eventually some other organic compounds or ammonia, forming a stable cluster. Those small, initial nucleation particles of 1-2 nanometers can subsequently continue growing.

Growth of aerosols can happen under different conditions, depending on the size and the chemical properties of the aerosol. Condensation of water to the aerosol is one of the largest factors causing growth, although other vapors (such as H_2SO_4) can also

condense on existing aerosol particles. The extent of the growth by condensation of water (called *hygroscopic growth*) is depending on the hygroscopicity of the aerosol particle, which is the capacity of aerosols to interact with surrounding water molecules at both sub-saturated and supersaturated conditions. Inorganic salts (e.g. NaCl and NH_4NO_3) can be aerosols as small, solid particles or as a larger solution, depending on the relative humidity and their points of deliquescence. For example, the NaCl aerosol has a point of deliquescence at a RH of about 76% (Wise et al., 2007), meaning that from RH > 76%, the NaCl aerosol absorbed enough water to dissolve in it and to form a solution. When the RH drops below 76%, the NaCl aerosol will however not directly return to its solid state, since its point of efflorescence is at a RH of around 45% (depending on the size of the particle in dry state (Gao et al., 2007)). This inequality in the point of deliquescence and efflorescence poses the problem of hysteresis (the dependence of the state of a system on its history). When a RH of 60% is being measured and when having only data about the deliquescence and efflorescence point of a system, it is not possible to know which state the aerosol will have. In the case of NaCl it can either be solid or in a solution.

Hygroscopic growth over water and ice

A high relative humidity can thus cause a hygroscopic growth of aerosols and can lead to the formation of water clouds. In the Arctic environment, cold air temperatures can also cause aerosols to act as ice condensation nuclei (IN), forming ice clouds. This can happen at high values of the relative humidity over ice (RH_{ice}). The RH_{ice} is defined as the relative humidity with respect to a plane surface of ice and different from the RH_{water} under the same conditions, since saturation mixing ratios over ice are lower than over water (Wallace and Hobbs, 2006b). The RH_{ice} can be calculated by the Goff and Gratch equation, which is an experimental correlation that estimates the saturation water vapor pressure at a given temperature (Goff and Gratch, 1946). Two slightly different equations exist, one for above a flat surface of water and one for above a surface of ice, and the equations are applicable for -100°C < T < 0°C.

More detailed information on the quantification of hygroscopic growth will be presented in section 1.5

1.2.2 Optical properties

(*The information for this subsection mostly comes from the presentation of Christoph Ritter (C. Ritter, 2019)*.

The size, the shape and the refractive index of a particle are important for the radiative effects the aerosol exerts. Incoming light on an aerosol can be absorbed and scattered. In case of absorption, the incoming light loses its energy completely to the particle and is not being scattered. In case of scattering, the incoming light does not lose any energy (elastic scattering) or it does lose some energy and changes wavelength (Raman scattering). The sum of the absorption and the scattering is called the extinction:

$$\alpha = \sigma + a \tag{1.1}$$

, in which α is the extinction (in m^{-1}), σ is the scattering (in m^{-1}) and a is the absorption (in m^{-1}).

The aerosol optical depth (AOD) is a measure of the extinction of solar light by aerosols. It reflects the amount of direct sunlight not reaching the surface, by integrating the extinction of the whole vertical column on the atmosphere:

$$AOD = \int_0^\infty \alpha(z)dz \tag{1.2}$$

The AOD is dimensionless and depends on the wavelength. At a wavelength of 500 nm, an AOD smaller than 0.05 corresponds to clear conditions, an AOD of more than 0.1 indicates hazy conditions. Some regions, for example regions around the Sahara or some very densely populated areas can reach values up to 1.0 (due to dust storms and human-produced air pollution) (E. O. NASA, 2020).

Dependent of the size of the particle the light collides with, different scattering processes and therefore different extinction efficiencies can occur. The collision of light on aerosols differs from the collision of light on gases and nanoparticles (<10 nm), for which scattering called “Rayleigh scattering” occurs. The efficiency of this scattering is proportional to the wavelength by λ^{-4}, which is why blue light (with a smaller wavelength) is scattered more strongly compared to red light. On larger particles, the scattering is more complicated and generally has a smaller wavelength dependence.

Knowledge about the absorption, scattering and extinction of aerosols is important in order to estimate the direct effects on the radiative forcing in the climate system. Generally, the term albedo is being used to describe the proportion of the incoming radiation that is being reflected. For particles, the term single-scattering albedo (ω) is often used and describes the ratio of the scattering to the total extinction:

$$\omega = \frac{\sigma}{\alpha} \tag{1.3}$$

An ω of 1 implies that the extinction is fully due to scattering, an ω of 0 however that it is completely due to absorption.

The optical properties of the aerosols are however not only important to estimate the radiative effects but form the basis for many measuring techniques too. The Lidar technique for example, which will be highlighted below in more detail, relies on the backscattering (β) of the particles, which is defined as the light that is scattered back in 180°:

$$\beta = \sigma_{180^\circ}[m^{-1}sr^{-1}] \tag{1.4}$$

1.3 Remote aerosol measurements by Lidar

(*The information for this section mostly comes from the book of Weitkamp, 2005*). Different aerosol properties can be measured with different instruments. The types of measurements can be roughly divided into two categories: *in situ* measurements and remote sensing. Whereas *in situ* measurements are used to determine which aerosol is present and in what amount, remote sensing measures the optical properties of the aerosol. Remote sensing can be divided into two other subcategories: active and passive remote sensing. Active sensors have their own source of energy and emit radiation in order to illuminate the objects to be observed. The radiation that is then reflected or backscattered from the target objects can be measured. Passive sensors do not use such energy source and only measure the naturally reflected or emitted radiation from the object they observe (mostly reflected or backscattered sunlight) (E. NASA, 2020).

The Lidar (light detection and ranging) is an instrument belonging to the group of active remote sensing instruments and can be used for a wide range of goals, including measuring temperature, wind, trace gas concentrations and aerosols. In this work, the focus is on the measurement of aerosols. The Lidar sends out pulses of light and measures the light that is being backscattered by the particles in the atmosphere. The difference in time between the emitted laser pulse and the backscattered light gives the height at which the backscattering object (the aerosols) are, according to the following relation:

$$z = \frac{c}{2t} \tag{1.5}$$

, in which z is the height, c is the speed of light and t the time between the laser pulse and the recorded backscattered light. The factor two is included for the way for- and backwards (up to the point of the backscattering and then back to the telescope).

A Lidar system is being shown in figure 1.4. A laser emits a light pulse after retrieving a trigger signal from the transient recorder. This light pulse consists of the fundamental (1064 nm), second (532 nm) and third (355 nm) harmonic wavelengths. After emission, the pulse is being widened by the beam widening telescope (BWT) in order to reduce beam divergence and influences from background light at higher altitudes (Atmospheric Physics, 2020). The backscattered light is consequently being measured by a recording telescope (in this case consisting of one parabolic and one plane mirror). To reduce the pollution of the signal by sky background light, a field stop is being placed in the focal plane of the recording telescope, decreasing the field of view (fov) of the telescope and thereby excluding more background noise and increasing a signal-to-noise ratio. The collimating lens after the field stop parallelizes the incoming beam. Behind the lens a dichroitic mirror separates the different wave lengths and interference filters (IF) reduce the effect of noisy background light. In case of polarized light, the polarizing beam splitters (PBS) can separate the parallel (p) polarized light from the perpendicular (s) polarized light (both respective to the laser light). After the IF (and optionally after the PBS), the light is recorded in photomultiplier tubes (PMT). The electrons produced from the PMTs are then counted in a transient recorder.

The detection of the different backscattered wavelengths as well as the different polarization states from the Lidar allow to distinguish between different sizes and shapes of aerosols respectively. The quantity in which the caught signal is measured in the telescope, is called the returned power P. It includes all the light that is being scattered back into the telescope with an effective surface defined as A/z^2. However, part of the photons of the laser will be lost due to extinction by the other particles in the atmosphere on the way from 0 towards z and backwards. The extinction can be expressed by Beer-Lambert law. Additionally, technical factors such as the laser power, optical properties and PMT efficiency need to be accredited for in a Lidar constant C and an overlap function $O(z)$ is needed to correct for the laser light that actually is in the field of view (fov) of the telescope.

Taking these factors into account, an expression of P(Z) can be written as follows:

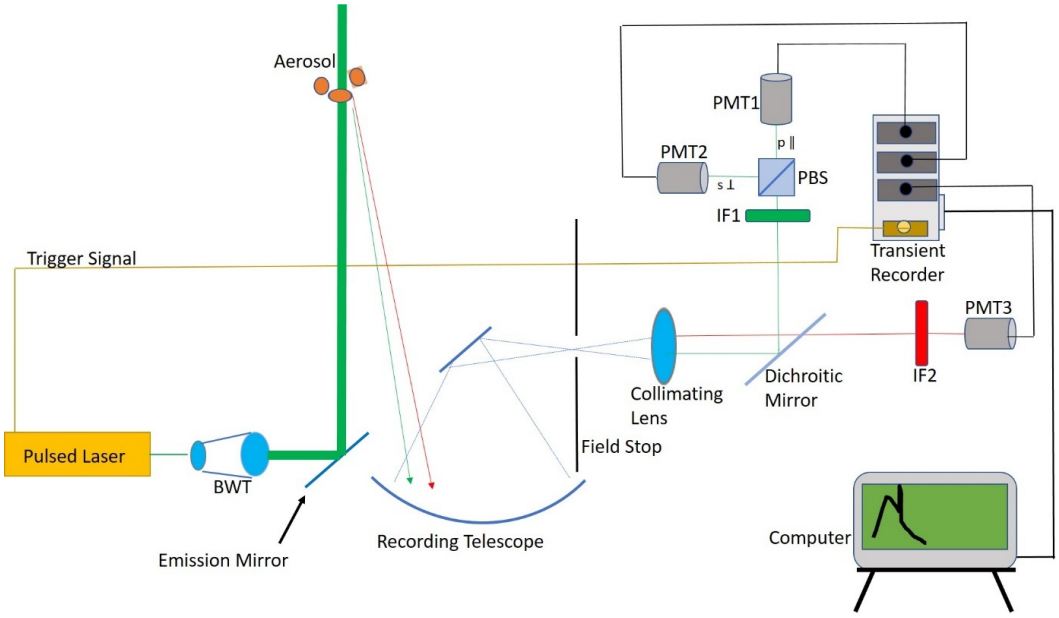

Fig. 1.4: A schematic overview of the KARL Raman Lidar.

$$P(z) = C\beta(z)\frac{1}{z^2}\exp(-2\int_0^z (a_\lambda(\hat{z})d\hat{z})) * O(z) \tag{1.6}$$

, in which $P(z)$ is the returned power P depending on the height z, c is the Lidar constant and β (z) the backscattered light over the height z. The part in the exponent represents the extinction (α) integrated over the height z and backwards (thus the factor 2). $O(z)$ is the overlap function.

1.3.1 Elastic scattering

Considering elastic scattering (as explained before), the elastic Lidar equation can be defined as in equation 1.6, since only one wavelength is being considered.

A similar equation can be made for Raman-scattering and is as follows:

$$P_r(z) = C_r\rho(z)\frac{1}{z^2}\exp(-2\int_0^z (a_{\lambda_e}(\hat{z}) + a_{\lambda_r}(\hat{z})d\hat{z})) * O(z) \tag{1.7}$$

The strongest Raman return is obtained from nitrogen molecules and is proportional to the air density (ρ) of the considered species (in mol/m^3). In equation 1.7, this Raman-shifted wavelength (λ_r) needs to be considered for the extinction as compared to the elastic Lidar equation (λ_e).

In case a Raman-channel is available, the equation can be solved for the extinction. In case green light is emitted, Raman scattering on N_2 particles occurs and light with a lower energy and a wavelength of 607 nm is being reflected. Scattering on gas particles is proportional to λ^4. Rayleigh scattering is proportional to the gas molecules and thereby to the density (ρ). The unknown terms in the equation are the aerosol extinctions. The extinction of the 532 nm light before the Raman scattering and the extinction of the 607 nm after scattering is therefore proportional to the Ångström exponent Å in the following way:

$$\alpha_{aer(532)} = \alpha_{aer(607)} * (\frac{532nm}{607nm})^{\text{Å}} \tag{1.8}$$

Using this relation, an equation for α_{532} can be made:

$$P^{607nm}(z) = \hat{C}\rho(z)\frac{1}{z^2}\exp(-2\int_0^z (f * a^{532}(\hat{z})d\hat{z})) \tag{1.9}$$

The solution for α_{532} can then be used for solving the elastic Lidar equation, which will be highlighted below.

Solving the elastic Lidar equation

The elastic Lidar equation involves two unknowns: the backscatter coefficient $\beta(m^{-1}s^{-1})$ and the extinction coefficient $\alpha(m^{-1})$. If a Raman channel is available and the inelastic solution for the extinction has been calculated, this extinction can be used in the elastic equation. The backscatter will then be the only variable left and the equation can be solved for the backscatter. However, if the Raman channel is not available, solving the elastic Lidar equation with its two unknown components is not so trivial and will be explained below.

The total backscatter coefficient β and the extinction coefficient α are formed by the contribution of the aerosols as well as the gases:

$$\beta^{tot} = \beta^{Ray} + \beta^{aer} \tag{1.10}$$

$$\alpha^{tot} = \alpha^{Ray} + \alpha^{aer} \tag{1.11}$$

α^{Ray} and β^{Ray} are known from the radiosonde data, which is why α^{aer} and β^{aer} are the unknowns.

The first step in solving the equation is to relate α and β by using the Lidar Ratio (LR) and writing it in the following way:

$$LidarRatio : LR_{532nm}(z) = \frac{\alpha^{aer}}{\beta^{aer}} \tag{1.12}$$

The Lidar ratio now allows to write the term α^{aer} in terms of β^{aer} and the Lidar ratio. However, the Lidar ratio can be set fixed for different types of aerosols. Usually, the Lidar ratio of cirrus clouds or sea salt aerosol is in the range of 10 sr, although soot will have a Lidar ratio in the range of 100 sr. Rewriting the equation for β^{aer} and having the Lidar ratio as a set number and not as an unknown term, yields the following equation:

$$P * z^2 \exp(+2 \int_{z_0}^{z} (a^{Ray} - LR\beta^{Ray} d\hat{z}) = C\beta^{tot} \exp(-2 \int_{z_0}^{z} (LR * \beta^{tot} d\hat{z}) \tag{1.13}$$

This equation then is a differential equation for β^{tot} and can been solved by first rewriting the equation into a non-linear differential equation which can be transferred into a linear differential equation using the Bernoulli substitution. Solving the resulting linear differential equation is then being done using the method James Klett (1981) proposed. He stated that the integration has to be done from the far side of the system backward and for that, a boundary condition for β^{tot} (z_{ref}) has to be defined. By doing so, the differential equation for β^{tot} can be solved with β^{tot} as the only unknown.

Parameters to be determined

The solution of β^{tot} (and therefore β^{aer} too) allows the determination of some parameters that can roughly define the aerosols particles.

The backscatter ratio (BSR) is usually given as the ratio between all the backscatter measured and the Rayleigh backscatter that can be attributed to the gases in the air and is defined as follows:

$$BSR(\lambda) = \frac{\beta^{aer}(\lambda) + \beta^{Ray}(\lambda)}{\beta^{aer}(\lambda)} \tag{1.14}$$

A BSR of 1 indicates a clear sky, whereas when BSR $>$ 1, aerosols particles are in the air.

The color ratio (CR) gives some rough information about the size of the aerosols. It is defined as the aerosol backscatter ratio of two different colors (and is therefore determined from multi-wavelength Lidar data):

$$CR(\lambda_1, \lambda_2) = \frac{\beta^{aer}(\lambda_1)}{\beta^{aer}(\lambda_2)} \tag{1.15}$$

It is determined that $\lambda 1 < \lambda 2$. Shorter wavelengths are more strongly backscattered than longer wavelengths and therefore CR is $>$ 1. In case of a high prevalence of small aerosol particles and an Angström exponent of -4, the CR can reach the Rayleigh limit of $\frac{\lambda_1}{\lambda 2}^{-4}$ (or $\frac{\lambda_2}{\lambda 1}^{4}$). However on large particles with an $Angström$ exponent reaching 0, the CR with approximate a value of 1.

The depolarisation ratio as an indicator of the shape of the aerosols and is defined in the following way:

$$\delta^{aer}(\lambda) = \frac{\beta_{\perp}^{aer}(\lambda)}{\beta_{\parallel}^{aer}(\lambda)} \tag{1.16}$$

The Lidar emits polarized light. Mie theory states that spherical particles do not change the state of polarization upon backscattering, although non-spherical particles do so. The ratio between the depolarized backscattered light and the not-depolarized scattered light therefore functions as a shape indicator.

1.3.2 Challenges with Lidar data

In analysing Lidar data, a challenge in the trade off between the overlap and the width of the aperture is present. As stated before, the Lidar has a field stop in the focal plane in order to decrease the field of view (fov). This has the advantage of limiting the effect of background noise in the recorded data. However, by introducing a field stop, some rays of the edge of the telescope will be blocked and therefore not the full telescope is involved in the formation of the image (see figure 1.5).

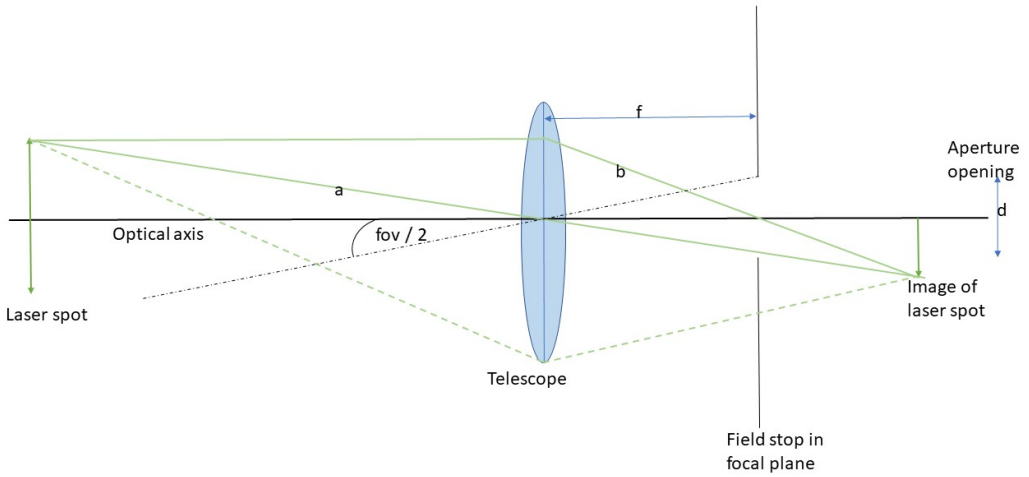

Fig. 1.5: The overlap issue in the Lidar - part 1.

However, the image of the laser needs to be in the view of the telescope completely. At very low height, the overlap - written as the overlap function $O(z)$ - is 0, but higher up in the atmosphere, the overlap increases until $O(z)$ reaches 1: this is the height at which the laser beam and the fov fully overlap and is called the overlap height ($z_{overlap}$). From this height on, the data of the lidar are usually used. The height from 0 to $z_{overlap}$ is therefore the "blind spot" of the Lidar and is not being taken into account.

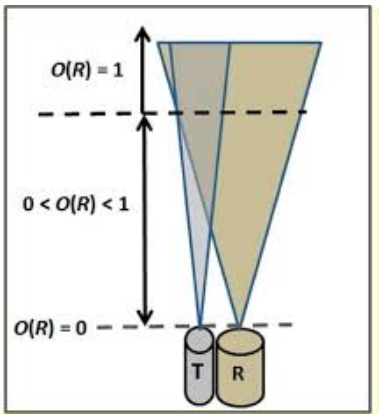

Fig. 1.6: The overlap problem in the Lidar - part 2.

Widening the field stop in the focal plane will cause a lower $z_{overlap}$ (and therefore a smaller blind spot), it will cause however more background noise. Inversely, narrowing the field stop causes less background noise, but the blind spot of the Lidar will be larger.

1.4 Meteorology and aerosols over Ny-Ålesund, Spitsbergen

As stated before, this master thesis will evaluate the Lidar data from January to March 2019 over Ny-Ålesund, Spitsbergen (78°55'24"N, 11°55'15"E) 1.7.

Fig. 1.7: The location of the research village Ny-Ålesund (NPI, 2020).

1.4.1 The polar vortex and transport regimes

Ny-Ålesund is situated in the northwest of Spitsbergen. It is directly situated to a fjord on its north side and is surrounded by mountains in the south. From a climatological and a meteorological point of view, it is under an influence of warm, wet marine air coming from the south and south-west (over the Norwegian Current and the West-Spitsbergen Current) and of cold polar air coming from the north. Contact of those air masses causes cyclonic circulations, causing a changeable weather in the Spitsbergen region. In winter and early spring, the polar vortex is pronounced and influences the meteorology strongly. The polar vortex is an upper-level low-pressure system situated above both the Arctic and the Antarctic. The low-pressure system occurs starting in the middle/high troposphere, reaching into the stratosphere. The air in the lower troposphere is dense and cold. The boundaries of the polar vortex are characterized by sloping isentropes, marking the interface between the cold, dry Arctic air and the warmer and moister air coming from the south. Due to the cold conditions in winter time, this contrast is stronger, and therefore the polar vortex is most distinct in the winter/early spring.

The distinct polar vortex in wintertime causes a transport barrier. The region affected by the polar vortex is then sometimes be called "polar dome" and is difficult to enter for other air masses (Bozem et al., 2019). During strong polar vortex events, two major transport pathways of air parcels into the lower Arctic troposphere are possible. The first is by low level transport of already cold air parcels into the polar dome (Klonecki et al., 2003). Those air masses typically come from North Asia, where the air masses travelled already over land (and snow) and has therefore been cooled down. When entering the polar dome, those air masses are cooled down further diabatically. A typical transport timescale for this type of transport is between 10 and 15 days. The second pathway involves air parcels coming from southern mid-latitudes. In those regions, fast uplift due to convection brings air parcels up to a high altitude, which are then being transported further north. Radiative cooling then causes the air masses to descent slowly into the polar dome area, where it will be cooled down further. This transport pathway is common for air masses coming from North America and East Asia (Stohl, 2006).

1.4.2 Aerosol parameters and composition

Generally, Arctic aerosol concentrations are very low (around a few hundred particles per cm^{-3}), whereas in rural areas in the mid-latitudes values can reach up to a couple of 1000 particles per cm^{-3} and up to 10000 particles per cm^{-3} in more densily populated areas (reaching even higher values in some cities)(DWD, 2020). Measurements of (tropospheric) aerosols have been performed in Ny-Ålesund for multiple years by different stations and different instruments. Seasonal variations have been described in both the amount and the type of aerosols. The general trend seen is the presence of Arctic haze, which is at its strongest in early spring (Quinn et al, 2007). Generally, the most common type of aerosols found in the Arctic are sulfates. During Arctic haze events, those sulfates increase significantly and make up around 30% of the submicron aerosols. A few different studies with different measuring techniques will be presented in chronological order here. There are some variations in the data, but the presence of the Arctic haze event and the domination of sulfates is consistent during the different studies.

Hara et al. (2003) conducted an airborne campaign in 2000 (end of March/beginning of April) above Spitsbergen, focusing on Ny-Ålesund. Different aerosol observation instruments were mounted in the research plane, including an Aerosol Impactor Sonde (AIS). With this instrument, aerosols were collected and could later in the laboratory be studied further. In almost all layers of the troposphere (measured between 0 and 8000 m), sulfates were the largest contributor of aerosols. In the first 1000 m though, sea-salt was at some days the most prevalent (40% relative abundance). Other frequently seen aerosols were sulfates in combination with

soot, which were under hazy conditions . typically mixed externally, whereas under background conditions internal mixing was most prevalent. Depending on the height and the day, the different types of aerosols had different relative abundances.

Tunved et al. (2013) assessed aerosols both quantitatively and qualitatively at Zeppelin station, Ny-Ålesund, over a period of 10 years (from 2000-2010). In March, the number size distribution showed particle sizes between 10 and 1000 nm, with a peak around 300-400 nm (measured with a DMPS, a Differential Mobility Particle Sizer). Seasonal variations were observed as well. In January to April, most of the prevalent aerosols were around 100-500 nm, whereas from May to August, smaller aerosols (between 10 and 100 nm) were observed. This indicates the nucleation of new aerosols under influence of the permanent daylight in those months.

Ritter et al. (2016) examined the aerosol properties based on Lidar data for Ny-Ålesund in April 2014. The most dominant aerosol species were sea salt and sulfates. Highest aerosol backscatter profiles were seen in the lowest considered height from 1000-1500 m. Typical values for β^{aer} were between 0.3-0.6 m^{-1} sr^{-1} for 1000-1500 m, decreasing over height to 0.1-0.2 m^{-1} sr^{-1} between 2500-5000 m. Comparison with the CR showed a clear correlation of the aerosol backscatter and the size of the aerosols. Typical values for the LR were between 30 and 50 sr, yet the values were not stable. Aerosol depolarisation values were between 2 and 3%.

Willis et al. (2018) performed aircraft-based measurement (the NETCARE/PAMARCMiP 2015 campaign) of aerosols in the Arctic region too in early April, covering different research stations on Spitsbergen, Greenland, and Northern Canada. Vertical variability in aerosol types during the campaign was observed. In the coldest air masses, the sulfate mass fraction was the highest (74%), whereas in higher temperatures the mass fraction of organic aerosols increased (up to around 42% in the upper polar dome air mass, thus where it was warmest). Black carbon (BC) made up around 2% of the aerosol air mass in the upper polar dome, ammonium up to 7%. Lower polar dome air masses contained mostly sulfates and had smaller amounts of organic aerosols, black carbon and ammonium as the middle and upper polar dome. Also, NaCl was found in the lower altitudes, whereas in the higher altitudes the amounts of NaCl became so little, that they were neglectable. The NaCl particles were likely associated with an observed increase in larger accumulation mode particles. It has been seen before that sea salt comprises a significant part of observed aerosols at ground-based stations and reaches its highest concentrations in winter to early spring (as measured by e.g. Quinn et al. (2002) in Alaska). The sources of NaCl in wintertime are likely to be open leads in sea-ice /open sea water and wind-driven ice and snow processes, since those serve as local sources of aerosols (as shown by e.g. Held et al. (2011)). NaCl can also mix with sulfates at lower latitudes.

Shibata et al. (2018) performed Lidar measurements from March 2014 - March 2018 to see whether seasonal variation of aerosols could be detected. Highest AOD values were detected in late spring, reaching up to an AOD of 0.1 - 0.13 (depending on the chosen parameters). Measurements with a photometer by Herber et al. (2002) showed highest AOD values around the same time, however with a larger uncertainty: the upper limit was 0.18, whereas the lowest values did not reach higher than 0.04. Shibata et al. measured the highest aerosol concentrations in the lower troposphere (< 1 km) and the concentration decreased with one order of magnitude in a height of about 10 km. Typical found backscatter values from January to June in the first 2 kilometres are around 4 * 10^{-7} m^{-1} sr^{-1}, in February-March reaching up to values of 7 * 10^{-7} m^{-1} sr^{-1} around 600-700 m. From their Lidar data it was concluded that at that time the free tropospheric particles were likely composed of liquid phase sulfate and soot particles.

1.5 Determining hygroscopic growth of aerosols

There are several ways to assess hygroscopic growth of aerosols. One commonly used and for this study relevant parameter is the hygroscopic growth factor $GF(RH)$. This is defined as the ratio of the particle diameter at a high relative humidity $D_{wet}(RH)$ and the dry particle diameter D_{dry}:

$$GF(RH) = \frac{D_{wet}(RH)}{D_{dry}} \tag{1.17}$$

Another frequently used parameter is the scattering enhancement factor $f(RH, \lambda)$. The optical properties of aerosols change when growing hygroscopically and $f(RH, \lambda)$ can be used to describe the change of the aerosol light scattering coefficient (σ_{sp}):

$$f(RH, \lambda) = \frac{\sigma_{sp}(RH, \lambda)}{\sigma_{sp}(RH_{dry}, \lambda)} \tag{1.18}$$

, in which $\sigma_{sp}(RH, \lambda)$ depends on the relative humidity and the wavelength λ. Different studies have been performed in order to calculate the scattering enhancement factors on different sources of tropospheric aerosol. Zieger et al. (2010, 2013, 2017) performed research on the hygroscopic growth of particles in the Arctic troposphere (at the Zeppelin station in Ny-Ålesund, Svalbard from July-October in 2008) using the above mentioned parameters. In the study of 2010, Zieger et al. measured the aerosol light scattering coefficient $\sigma_{sp}(\lambda)$ as well as the backscatter coefficient $\sigma_{bsp}(\lambda)$ for different wavelengths and different RHs (between 20 and 95%) using a humified nephelometer and RHs below 20% with a dry nephelometer as a dry reference. With the $\sigma_{sp}(\lambda)$ data for different wavelengths and different RHs, f(RH)

could be calculated using equation 1.18 and a humidogram of $f(RH)$ was created in which the different values for $f(RH)$ were plotted against the relative humidity .

Those humidograms can be described by an empirical γ-model as has been used by e.g. Gassó et al. (2000):

$$f(RH) = (1 - RH)^{-\gamma} \tag{1.19}$$

, in which the γ is the hygroscopic growth factor per aerosol. An aerosol having a high hygroscopicity would have a large γ, whereas aerosols with low hygroscopicity would have a small γ. The empirical model has been plotted separately for a RH > 75% and a RH < 65%. A typical value found for $\gamma_{>75\%}$ was 0.58 for the aerosol at Zeppelin station and the campaign mean value of $f(RH = 85\%)$ was 3.24.

It is also possible to estimate the hygroscopic growth factor (GF) of the aerosol based on the chemical composition of the air, which will be done in the master thesis as well, using the chemical data from PM10-filters. This can be done using the Zdanovskii-Stokes-Robinson (ZSR) relation, using the hygroscopicity (water activity) of the volume fractions of the pure components in the aerosol following equation (Stokes and Robinson, 1966, Gysel et al., 2004):

$$GF_{mixed} = (\sum_{k} \epsilon_k GF_k^3)^{1/3} \tag{1.20}$$

1.6 Aim of this master thesis

This master thesis aims to determine the physical properties and the hygroscopic growth of aerosols from January to April 2019 in Ny-Ålesund, Spitsbergen using Lidar data and *in situ* data. Additionally, the challenges and opportunities of comparing data sets from Lidar and *in situ* instruments will be assessed.

In the first part of the presented results in this thesis, an overview of some physical aerosol properties averaged over the whole period of January to April will be given, considering the backscatter at 532 nm, the color ratio CR and the depolarisation ratio at 532 nm. Those properties will subsequently be investigated per month to check for a temporal difference in properties.

To determine the hygroscopic growth, some days will be studied specifically which have a clear vertical relative humidity gradient in the first 5 km of the troposphere and which have Lidar data available at the same time. This will be done by plotting the backscatter data of the Lidar against the relative humidity measured by the

radiosonde and like this, the presence of hygroscopic growth can be observed. When this is being observed, the empirical γ-model as proposed by Gassó et al. (2000) will be fitted for different values of gamma. The first aim of this specific experiment is therefore to investigate which γ-value fits best to the plots and what type of aerosol this indicates. A second aim is to discover how well the γ-model can be applied for Lidar data. The γ-model as applied by Zieger et al. (2010) was being fitted through scatter data measured by an *in situ* system in which the relative humidity was well controlled. In this master thesis, not scatter- and RH data from an *in situ* system, but backscatter data from an Raman Lidar and RH data from a weather balloon are available and will be used to fit the γ-model. It is likely that those data sources will have a larger errors, making it more difficult to determine a clear γ-value.

Apart from determining the properties and hygroscopic growth of aerosols based on Lidar measurements, some *in situ* data will be used as well to get a fuller overview of the aerosol properties and to determine differences in the methods. For all days for which a growth curve based on Gassó et al. (2000) is calculated, a growth factor and γ-value will be calculated based on *in situ* data using the ZSR-relationship. Those *in situ* (PM10-filter) data are ground-level aerosol concentrations in μg/m^{-3}.

For the 19th of January, the existing Lidar data is supplemented with *in situ* aerosol size distribution data at altitudes of 0-700 m and a hygroscopic growth factor based on the PM10-filter measurements can be made as well.

Not a lot of literature exists on comparing results of *in situ* and Lidar data and apart from determining the aerosol composition from January to April 2019, this master thesis aims to highlight the difficulties and the possibilities of comparing different data sets. Combining optical and chemical methods can be a step closer to bringing together different disciplines on aerosol analysis and a step closer to a better understanding of the Arctic aerosol composition and development.

2 Data and methods

Different data sets and evaluation methods have been used for this study. In the following section the way the data sets have been obtained and evaluated will be explained.

2.1 Overview of the measuring sites

Radiosonde, Lidar and *in situ* data have been used for this master thesis. Those data have all been retrieved in Ny-Ålesund, however not at exactly the same sites. Figure 2.1 shows the village of Ny-Ålesund, indicating the relevant buildings for this study. Lidar data have been obtained in the AWIPEV observatory (1 on the map) and radiosonde data come from weather balloons which were launched in the balloon house next to the observatory (2). Both facilities belong the the French-German research station AWIPEV in Ny-Ålesund. The *in situ* PM10-filter data come from the observatory "Gruvebadet" (3) and have been operated by Italian researchers from the national research council of Italy and the university of Firenze. Gruvebadet is situated around 700 m away from the AWIPEV observatory.

2.2 Evaluation of Lidar and radiosonde data

In the introduction 1.3, the principle of the Raman Lidar technique and the mathematics behind it have been explained already. The specific Lidar used in Ny-Ålesund is called KARL, the Koldewey Aerosol Raman Lidar. The laser beam of this Lidar consists of three wavelengths: 355 nm (ultraviolet), 532 nm (green) and 1064 nm (infrared). The telescope captures the backscattered light at those wavelengths and additionally at 387 nm and 607 nm by its Raman channels. The conversion of the raw Lidar data and the isolation of the different parameter of interest, has been done with a Matlab script by Christoph Ritter. Since a Raman channel is available, the elastic Lidar equation can be solved by both using the extinction α_{532} (being calculated using the equation for Raman-scattering) and by introducing a Lidar Ratio. Both methods have been integrated in the Matlab script. The values for α^{Ray} and β^{Ray} have been obtained from air density profiles from radiosonde data.

Fig. 2.1: Overview of the relevant measuring sites in and around Ny-Ålesund.

The data were evaluated in a temporal resolution of 10 min and a vertical resolution of 30 m. Subsequently, the data were analysed for false values due to not-homogeneous technical settings (due to miss fitting Lidar ratios or different overlap functions) by looking at abnormal data patterns in contour plots in which the BSR has been plotted over time and height. Abnormal data could either be corrected by changing the technical settings or have been left out in the analysis. After filtering the data in this manner, 1295 time steps (of 10 min) from January to April were left over for the analysis. Next, the data were filtered for clouds, since only clear sky measurements were used. All data points corresponding to β^{Aer} (532 nm) $> 2 * 10^{-6}$ m^{-1} sr^{-1} or CR (355 nm, 532 nm) < 2 were ignored.

Radiosonde data were obtained from (at least) daily launched weather balloons at the AWIPEV station. The radiosondes used are the type RS-41 from Vaisala. Apart from the air density profiles of the radiosondes, their relative humidity measurements have been used extensively for the determination of hygroscopic growth. From the Lidar measurements, the mass mixing ratio of water in air can be calculated as well. However, previous research (Kulla and Christoph Ritter, 2019) shows that this works well at night (in darkness), but that the accuracy drops during Lidar measurements in daylight. Therefore, the relative humidity data measured by the radiosondes were used.

2.3 Hygroscopic growth determination by Lidar data

In this study, the determination of hygroscopic growth requires the simultaneous availability of relative humidity data from the radiosondes and the Lidar data. As a first step in choosing the days used in a case study for determining hygroscopic growth, all Lidar data were selected that were in a $\pm$ 30 min time frame from a launched radiosonde. All relative humidity profiles from the radiosondes (for which at least one Lidar data set, so at least one time step was available) were then plotted against the height (up to 10 km) and first visually examined for strong gradients in relative humidity (from $>$ 80% to $<$ 40%). For those time steps and in the heights where the RH gradient was observed, the relative humidity was plotted against the aerosol backscatter, as well as against the aerosol depolarization to check for the possible formation ice crystals. Two days were selected that showed the presence of hygroscopic growth and those were used to plot the γ-curve.

Growth curves with gamma values between 0.00 and 1.50 with steps of 0.05 were fitted through all the backscatter data that corresponded with a certain higher value of the relative humidity (depending per day and time step, which is further shown in the results). The calculated f-values per curve were then normalized by dividing by the average value of f at drier relative humidity values (f_{dry}). β-values were normalized by dividing through the average value of β at drier relative humidity values (β_{dry}). For each time step, the best fitting curve was chosen based on the least squares approach, in which the difference between the normalized β-values and the normalized f-values were squared and summed. The γ-value corresponding to the best fitting curve was considered the value fitting the given composition of aerosols.

2.4 *In situ* data evaluation

For some days, *in situ* data were provided. *in situ* aerosol profile data from Mauro Mazzola and David Cappelleti (from the Italian research council in Bologna) from an optical particle size scanner (OPS) showed the number concentrations of particles for which D $>$ 0.3 micron. Those data were retrieved for the 19th of January from 11:10:30 until 12:19:30 in intervals of 30 seconds. No raw data, but a plot for the concentration of fine particles (14 nm $<$ D $<$ 300 nm) for the 19th of January was obtained from Mazzola as well. Additionally, meteorological data from the tethered balloon "Mozzarella" were available. One profile was obtained between 12 and 14h, the second one between 16 and 17h. The last obtained profile has not been

used though, since the analysis of those data showed false values. Probably it was forgotten to remove the cap covering the relative humidity sensor.

For all days, PM10-filter data were available from Rita Traversi (Dept. of Chemistry "Ugo Schiff", University of Florence). The PM10-filter system is situated at the Gruvebadet observatory and measures the ground-level total PM10 load as well as other chemical parameters. Samples were being collected every second day and one sample covered 48-hours (so it was measured continuously). From those data, the hygroscopic growth factor $GF(RH)$ has been calculated using the Zdanovskii-Stokes-Robinson (ZSR) relationship as mentioned in section 1.5. In order to compare the calculated $GF(RH)$ of the *in situ* data with the calculated $f(RH)$ based on the Lidar data, the $GF(RH)$ was transformed into $f(RH)$. Whereas the $GF(RH)$ indicates the change in particle *diameter*, the light scattering enhancement $f(RH, \lambda)$) is dependent on the increase in *surface* or on the increase in *volume* (depending on the used measuring technique). Since the calculated values for $f(RH)$ in the growth curves are based on Lidar backscatter values and since the strength of aerosol backscatter depends on the surface of the aerosols, it has been chosen to approach $f(RH)$ as GF_{mixed} squared:

$$f(RH) = (GF_{mixed})^2 \tag{2.1}$$

Like this, f-values (and their corresponding γ-values) can be calculated based on the growth factors of the *in situ* data and those can be compared with the resulting f- and γ-values from the Lidar data.

2.5 Overview of data availability and case study days

The following table shows the data availability of the Lidar measurements. It indicates which time steps are for which dates available. For January, most data are available, whereas for April only few data are available. In total, 1295 time steps were evaluated and used for the analysis.

Tab. 2.1: Overview of available Lidar data for January - April 2019. The blue marks indicate the dates for which the Lidar data is partly overlapping with the data from the radiosonde in a ± 30 min time frame. TS indicates the number of evaluated time steps per day, one time step includes 10 minutes.

Jan	TS	Feb	TS	March	TS	April	TS
09. Jan	9	01. Feb	5	05. Mar	22	01. Apr	28
11. Jan	33	05. Feb	9	07. Mar	60	04. Apr	7
12. Jan	2	06. Feb	87	21. Mar	22	06. Apr	31
13. Jan	4	07. Feb	40	22. Mar	15	07. Apr	27
14. Jan	28	08. Feb	46	23. Mar	44	08. Apr	2
15. Jan	12	09. Feb	70	25. Mar	10	11. Apr	19
16. Jan	3	10. Feb	19	26. Mar	11	21. Apr	2
17. Jan	30	11. Feb	22	27. Mar	4	30. Apr	26
18. Jan	45	12. Feb	13	28. Mar	16		
19. Jan	81	24. Feb	7	30. Mar	43		
20. Jan	73	25. Feb	19	31. Mar	39		
21. Jan	36						
22. Jan	47						
23. Jan	64						
25. Jan	8						
27. Jan	19						
28. Jan	42						
	536		337		286		142

3 Results

3.1 Aerosol properties averaged for January to April 2019

In order to get an overview of the aerosol properties from January to April 2019, the relative frequencies of different values of the backscatter at 532 nm, of the depolarisation ratio at 532 nm, of the color ratio and of the Lidar ratio at 355 nm were plotted. The data have been filtered for clouds, only the not-cloud affected data points have been taken into account. Appendix 1 shows the relative frequencies in numbers and shows which percentage of the data are represented in the graphs.

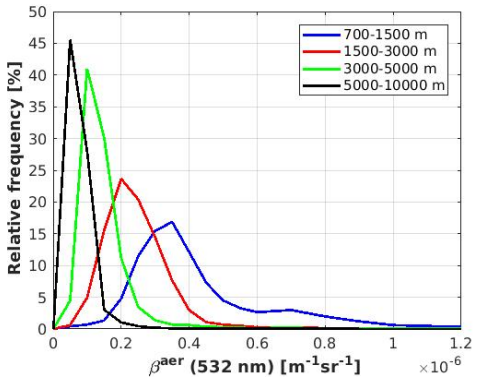

Fig. 3.1: Jan-Apr: Frequency of β_{532}

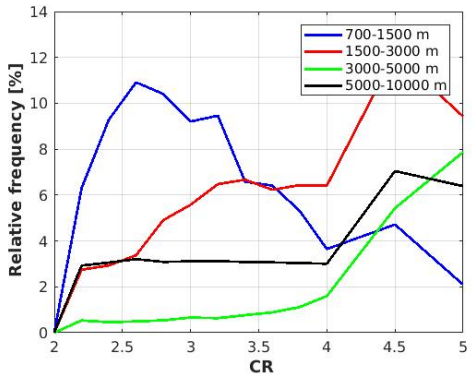

Fig. 3.2: Jan-Apr: Frequency of the CR

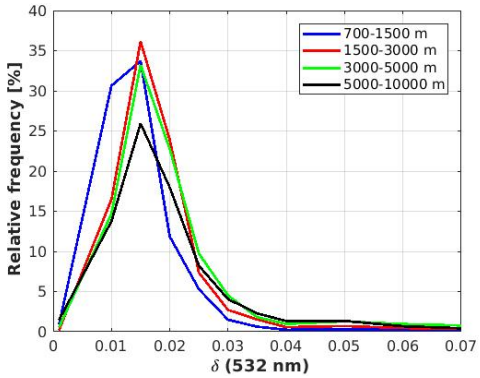

Fig. 3.3: Jan-Apr: Frequency of δ_{532}

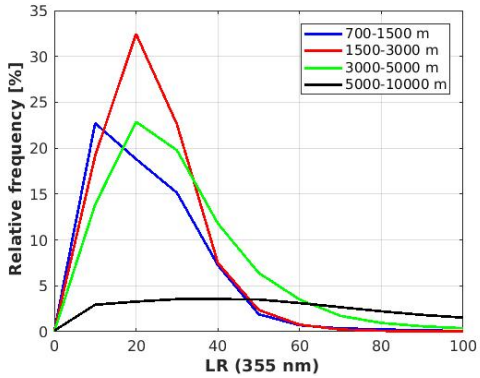

Fig. 3.4: Jan-Apr: Frequency of the LR_{532}

From January to April 2019, the highest backscatter (between 0.2 and 0.5*10^{-6} m^{-1} sr^{-1}) was observed between 700 and 1500 m, decreasing with the height. This indicates more and/or larger particles in the lower altitudes compared to higher altitudes. The color ratio shows large differences between the heights. Low CR values are observed between 700 and 1500 m , indicating larger particles, whereas larger CR-values are observed for 3000-5000 m and 5000-10000 m, indicating smaller particles. As mentioned in section 1.3, the CR can reach the Rayleigh limit of $\frac{\lambda_1}{\lambda 2}^{-4}$ when very tiny aerosol particles are present. This limit is at 5*10^{-6} m^{-1} sr^{-1}, which is why the graphs (also in section 3.2.3) were cut off at this value. From 3000 to 10000 m, the CR data showed many values higher than 5, which is why low relative frequencies are observed. This is due to noise and those data were not used for interpretation. In Appendix 1 to 5, all tables with the relative frequencies are shown as well as the percentage of data included in the graphs. The course of the depolarisation is similar for all heights, but small differences are visible. The interval 700-1500 m shows slightly lower depolarisation values (spherical particles), whereas between 5000 and 10000 m, slightly larger depolarisation values are present, indicating less spherical (potentially icy) particles. The observed Lidar ratio at 355 nm is mostly between 0 and 40 for the heights between 700 and 5000 m. Between 700 and 1500 m, the lowest Lidar ratios are observed, pointing at the presence of either icy particles or sea salt particles. Due to the low altitude, the presence of sea salt particles is likely. The LR between 5000 and 10000 m was too noisy for interpretation.

Since January involves most of the data points (and April the least), the graphs above are the strongest influenced by January, the least by April. To be able to distinguish the trends per month, the backscatter at 532 nm, the depolarisation ratio at 532 nm, the color ratio and the Lidar ratio at 355 nm will be shown per month and per height in the next section.

3.2 Aerosol properties per height

3.2.1 β_{532} per height

The relative frequencies for the backscatter at 532 nm for the four different height intervals are shown in figure 3.5 to 3.8 (and see appendix 2). Between 700 and 1500 m, the highest backscatter is seen in February, since a little "peak" is present between 0.6 and 0.8 *10^{-6} m^{-1} sr^{-1}. January and March look similar for this height interval, whereas in March, the backscatter does not exceed 0.6*10^{-6} m^{-1} sr^{-1}. Between 1500 and 3000 m, the backscatter peak for all months is around 0.25, although April shows slightly higher backscatter values than the other months. The backscatter peak between 3000 and 5000 m is for all months around 0.15*10^{-6} m^{-1} sr^{-1} and for 5000-10000 m around 0.1*10^{-6} m^{-1} sr^{-1}. The variation in the upper altitudes between 5000 and 10000 m is lower, whereas between 700 and 1500 m the variation is larger, potentially showing a larger influence by the surface than by the transport of air masses higher in the troposphere. Small differences in the backscatter are thus seen over the months, but no clear haze season is observed: the backscatter in March and April is not larger as in January.

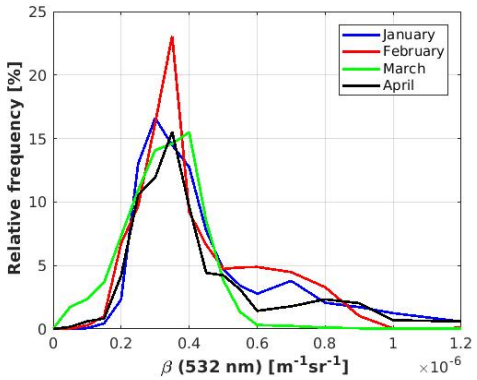

Fig. 3.5: 700-1500 m: Frequency of β_{532}

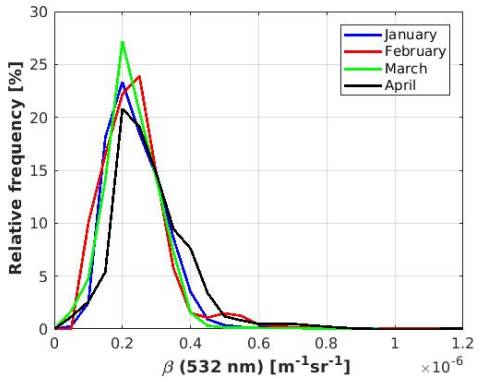

Fig. 3.6: 1500-3000 m: Frequency of β_{532}

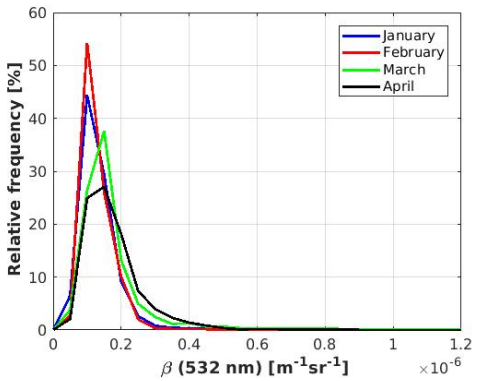

Fig. 3.7: 3000-5000 m: Frequency of β_{532}

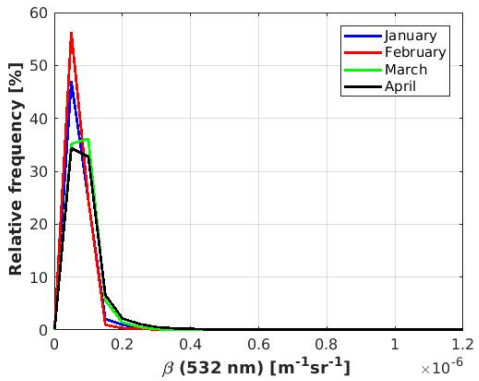

Fig. 3.8: 5000-10000 m: Frequency of β_{532}

3.2.2 δ_{532} per height

Considering the depolarisation ratio at 532 nm (see figure 3.9 to 3.12 and appendix 3), similar values between 700 and 1500 m for all months are seen with peaks between 1 and 2%. For 1500-3000 m, peaks between 1.5 and 2.0 % are observed. For 3000-5000 m, a sharp peak around 1.5% is visible for the month February, however especially in March and April the depolarisation shifts towards higher values of 3 and 4%. This trend continues in March and April for the altitude between 5000 and 10000 m, in which higher depolarisation ratios were seen. Especially in April, the depolarisation ratio reaches levels of 7% for this height. However, for January and February, the depolarisation peaks stay around 1.5%, although the peaks are less sharp and slightly higher depolarisation values are observed. More general it can be stated that the depolarisation in January and February is quite stable over the height and shows the presence of spherical-like particles (likely sulfate and ammonium particles), whereas March and especially April show larger changes in depolarisation over the height (higher values in higher altitudes), indicating the presence of less-spherical icy particles.

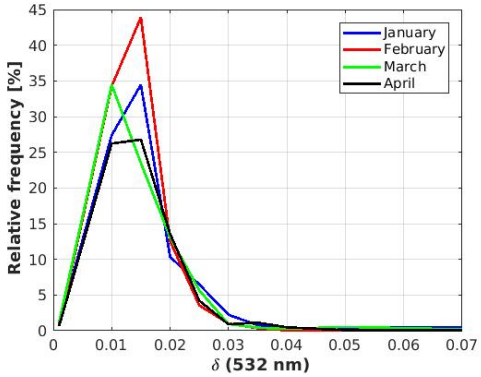

Fig. 3.9: 700-1500 m: Frequency of δ_{532}

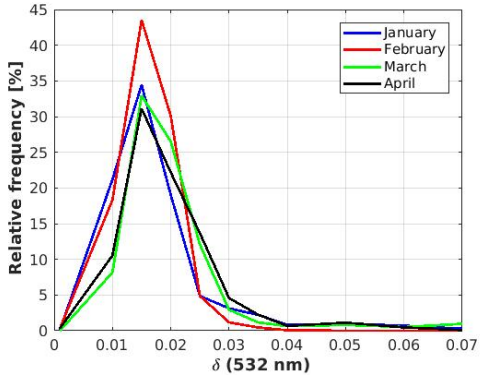

Fig. 3.10: 1500-3000 m: Frequency of δ_{532}

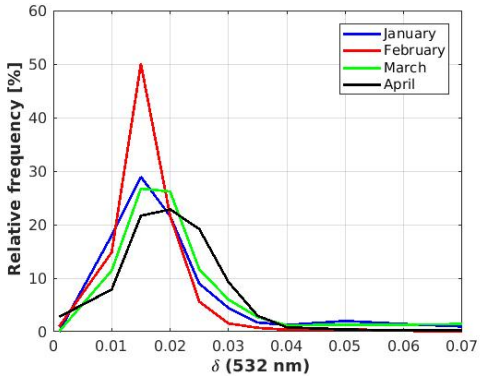

Fig. 3.11: 3000-5000 m: Frequency of δ_{532}

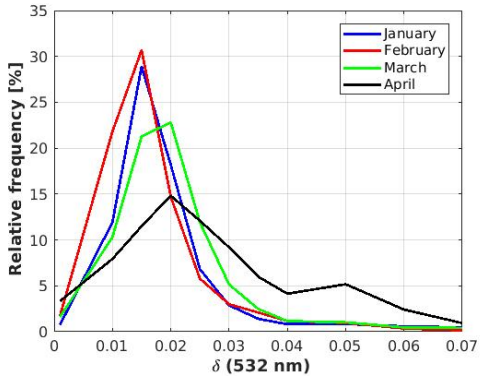

Fig. 3.12: 5000-10000 m: Frequency of δ_{532}

3.2.3 Color ratio per height

The CR shows different patterns for the height intervals 700-1500 m and 1500-3000 m (see figure 3.13 and figure 3.14 and appendix 4). Only those height intervals have been shown, since between 3000-5000 m and 5000-10000 m, the relative frequencies were too low, due to the fact that a part of the calculated CR-values were not taken into account because they exceeded 5. As stated before, this is due to the noise of the Lidar signal. Those height intervals have been shown though in the appendix.

It is seen that above 1500 m there is a dominance of very small particles, hence the focus will be on the 700 - 1500 m height interval (figure 3.13). For this interval, values of the CR over the whole range (between 2 and 5 m) are seen, however especially in February and March, a peak between 2.5 and 3 m is observed. In January, two little peaks are seen: one around a CR of 2.2, the other between 3 and 3.5. For 1500 to 3000 m, higher CR-values are seen for all months, indicating the presence of smaller particles in this altitude compared to 700 and 1500 m.

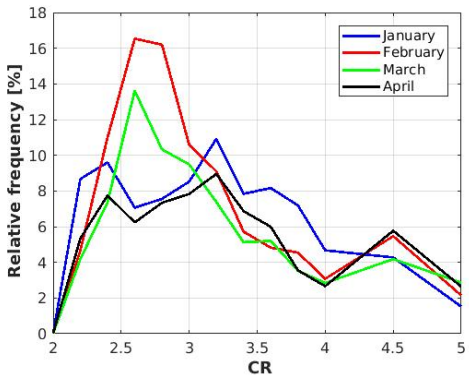

Fig. 3.13: 700-1500 m: Frequency of the color ratio

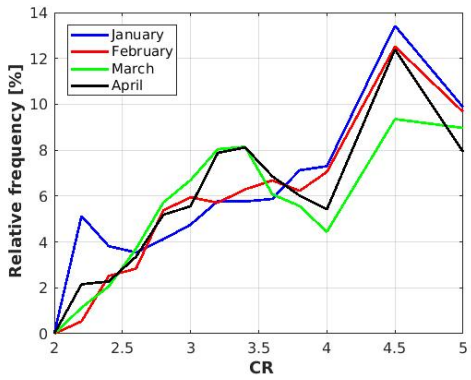

Fig. 3.14: 1500-3000 m: Frequency of the color ratio

3.2.4 Lidar ratio per height

The last optical parameter to consider is the Lidar ratio at 355 nm (see figure 3.15 to 3.17. In this case, the height interval 5000 - 10000 m has not been shown in here (but is however mentioned in appendix 5), due to the same reason as with the CR: a too large part of the data was not taken into account and therefore could not be used for interpreting.

Between 700 and 1500 m, the LR differs per month. Clear peaks were visible for January and February at a LR of 10 respectively 30 sr. In March, the peak was around 20 sr, whereas for April higher values for the LR (between 40 and 60 sr) were more frequently observed, indicating more soot-like aerosols in April and more sea-salt aerosols in January. For 1500-3000 m, more similar LRs were seen for all months, ranging mostly between 0 and 60 sr, although for the months April values up to 80 sr were observed. A similar graph is seen for 3000-5000 m, although the peaks are less sharp and generally higher LR values are observed (up to an LR of 100 sr). Over the months, it is seen that April shows higher LR values in all heights, indicating the presence of more absorbing particles. Lidar ratios also increase over height, indicating that soot particles are transported in the higher altitudes from lower latitudes, although aerosols such as sea salt with a low LR have more local sources directly from the surface.

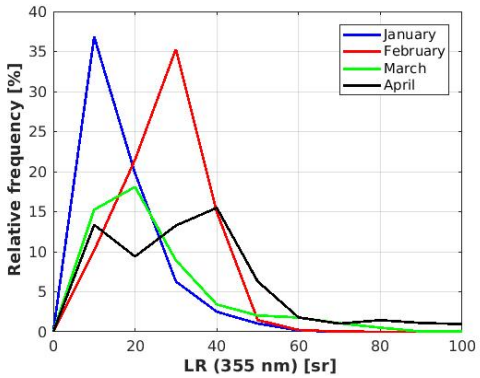

Fig. 3.15: 700-1500 m: Frequency of the Lidar ratio

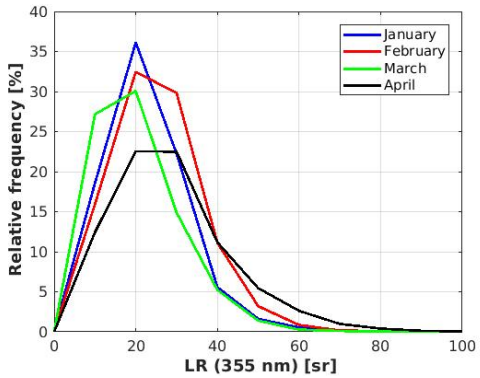

Fig. 3.16: 1500-3000 m: Frequency of the Lidar ratio

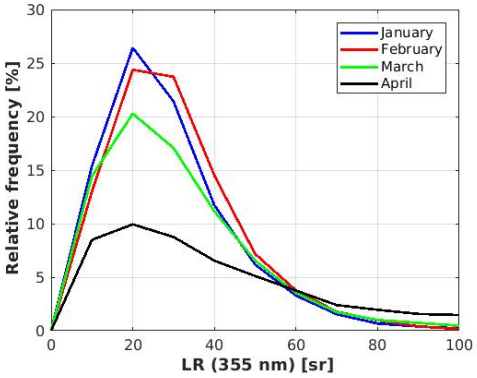

Fig. 3.17: 3000-5000 m: Frequency of the Lidar ratio

3.2.5 Relations between the parameters

The clearest relation between the optical parameters might be between the backscatter and the color ratio. An increase in backscatter can usually mean 1) *more* and/or 2) *larger* particles in the air. Since the color ratio is an indicator for the size, a smaller color ratio (larger particles) commonly goes hand in hand with a higher backscatter value. By looking at the graphs, this trend might be observed too for the data of this study. The highest backscatter was seen for the height interval 700-1500 m (peaking at 0.3 m^{-1} sr^{-1} and with values up to 1 m^{-1} sr^{-1}). For 700 to 1500 m, the color ratio showed the lowest values, indicating larger particles. To check for the correctness of this observation, the color ratio was plotted against the aerosol backscatter at 532 nm between 700 and 1500 m for all months (see figure 3.18). Based on this graph, one could say that for low values of β (< 0.5*10 $^{-6}$ m^{-1} sr^{-1}) no relation with the CR is observed and that both small and large particles are present, whereas for higher values of β (> 0.5*10^{-6} m^{-1} sr^{-1}), the presence of small particles decreases and only large particles (with a low CR) are present.

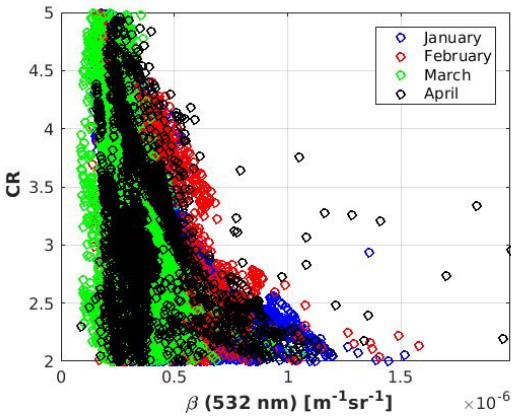

Fig. 3.18: The color ratio vs the aerosol backscatter for all months between 700 m and 1500 m.

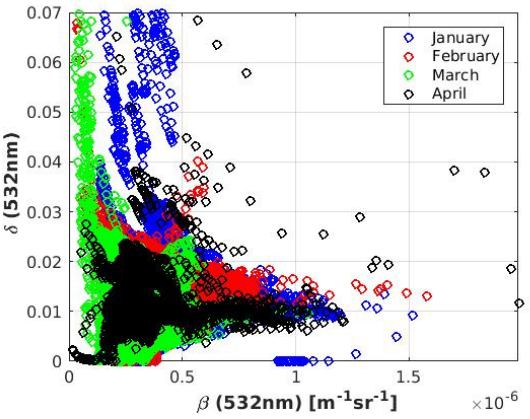

Fig. 3.19: The depolarisation ratio vs the aerosol backscatter for all months between 700 m and 1500 m.

To see whether the backscatter relates with the depolarisation ratio, the depolarisation ratio was plotted against β. A similar trend was observed as when comparing β with the color ratio. For low values of β (< 0.5*10^{-6} m^{-1} sr^{-1}) both higher and lower depolarisation ratios were being observed. For higher values of β (>0.5*10^{-6} m^{-1} sr^{-1}), mostly lower depolarisation ratios were observed, indicating spherical particles during more hazy conditions. The few cases in which the depolarisation was high, the backscatter was low. Due to the low backscatter, it is unlikely that those high depolarisation ratios belong to haze, but are more likely ice crystals. Combining this with the previous observation (high values of β correlate with low CR), it is likely that an increase in β correlates with larger and more spherical particles. The

CR has also been plotted against the depolarisation ratio and against the LR, but no clear trend was seen.

3.3 Hygroscopic growth

In order to investigate the hygroscopic growth of aerosols in Ny-Ålesund, it will be shown how the aerosol backscatter (at 532 nm) changes while the aerosols are being exposed to different values of the relative humidity. Theoretically, one could consider either the relative humidity over water or the relative humidity over ice to see how aerosols start growing hygroscopically. By looking at the depolarisation of the backscattered light (spherical particles such as in water clouds reflect less depolarised light than other shaped particles such as in ice clouds), previous research showed that the formation of ice clouds over Ny-Ålesund is a rare event and needs significant oversaturation over ice and low temperatures (Hoose and Möhler, 2012). Therefore it is unlikely that the occuring hygroscopic growth considered in this thesis comes from particles acting as ice nuclei. However, before only focusing on the hygroscopic growth by water, the possibility of the presence of ice nucleation should be considered for a more complete overview and will therefore be taken into account in the following section during the case studies.

Time frames between January and April 2019 where the data from the Lidar overlapped $\pm$ 30 min with the data from the radiosonde were selected to look for hygroscopic growth events. As a first step, for all those time frames between 700 and 10000 m (including 29140 data points, of which 9354 belonged to a RH of $>$ 50%), the backscatter at 532 nm was plotted against the relative humidity (see figure 3.20). Above 1500 m, no clear trend of hygroscopic growth could be observed by this. Between 700 and 1500 m, an increase in backscatter over RH was visible, but it is difficult to say whether this is hygroscopic growth. In order to find clear hygroscopic growth trends, one probably has to look at single events. In the data in figure 3.20, hygroscopic growth events might be present, but are covered by the amount of data.

For finding hygroscopic growth events, profiles for the relative humidity (over water) over height were plotted from 500 to 5000 m and examined for steep gradients in relative humidity (reaching from $>$80% to $<$40%). From the days for which a gradient in RH was found, the backscatter data were again plotted against the RH. The days which showed a hygroscopic growth trend were selected for further study. Those are the 28th of January and the 6th of February and those events will be shown in more detail in the next sections.

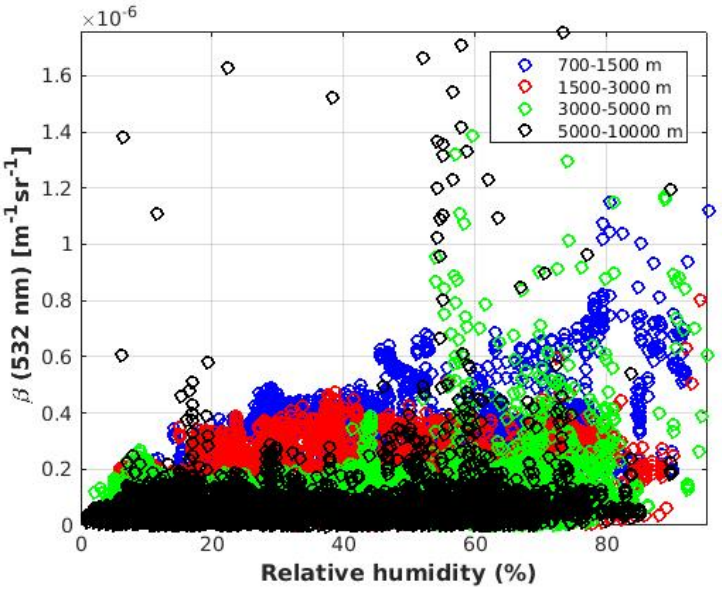

Fig. 3.20: β (532 nm) vs. the relative humidity between 700 and 10000 m height for all time frames between January and April 2019 in which the Lidar data overlapped $\pm$ 30 min with the launch of the radiosonde. The graphs consists of 29140 data points of which 9354 data points are above a RH of 50%.

3.3.1 Hygroscopic growth on the 28th of January, 2019

On the 28th of January, the radiosonde (launched at 16:45 UTC that day) measured a gradient in relative humidity from 80% towards 10% (RH over water) between 1700 m to 2500 m. As a first step, a contour plot for the whole day over the first 5 km of the atmosphere was made (see figure 3.21). The considered time- and height frame for this case study is shown by the red frame.

Lidar data from five time steps (at 16:25, 16:34, 16:47, 16:59 and 17:10) were used to study the hygroscopic growth of this event. It was seen that a decrease in relative humidity correlated with a decrease in BSR (see figure 3.22). Additionally, a decrease in BSR correlated with an increase in the depolarisation of the backscattered light (see figure 3.23). This might indicate the presence of spherical, larger particles in air with a high RH (due to water uptake) whereas aerosols in dry air are less spherical and smaller.

Because of this, only the relative humidity over water was considered and this was plotted against the aerosol backscatter at 532 nm (see figure 3.24). A hygroscopic growth curve was observed. Based on the paper of Zieger et al. (2010) (see section 1.5), a theoretical hygroscopic growth curve was plotted to the data. This was done based on the function $f = (1 - RH)^{-\gamma}$. Multiple fits for different gamma-values (ranging between 0 and 1.5 in steps of 0.05) were created and the function with the best fitting gamma was selected for the concerned time step (see section 2).

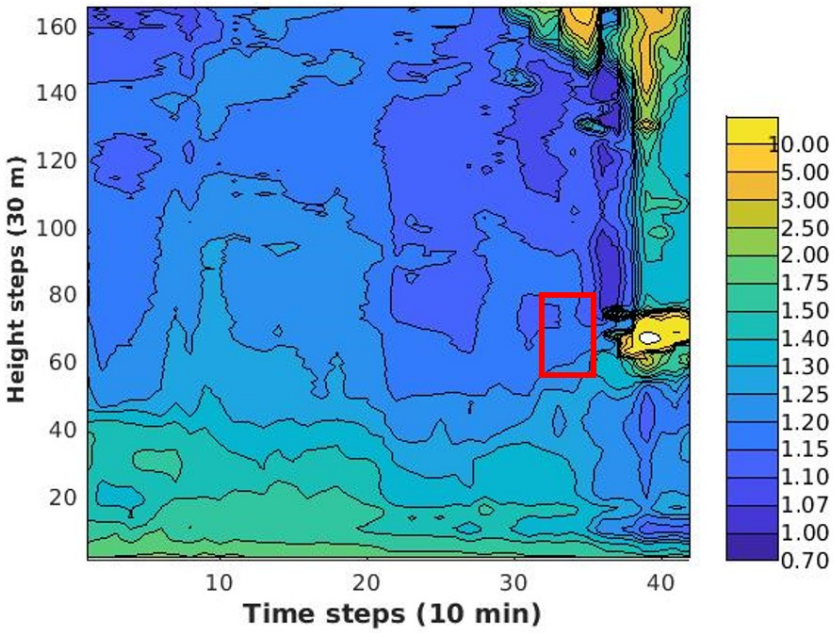

Fig. 3.21: A contour plot of the BSR belonging to the 28th of January. The x-axis represents the time steps, starting at 07:22 and ending at 18:18. The y-axis represents the height steps starting a 0 m, ending at 5015 m. The red frame shows the time- and height frame of this case study.

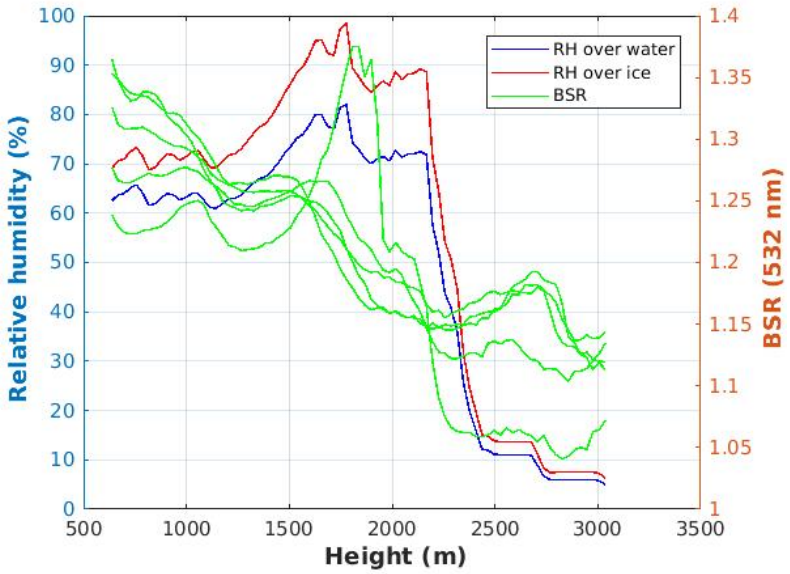

Fig. 3.22: The relative humidity profiles over water and ice (respectively blue and red) and the BSR at 532 nm (in green) between a height of 600 to 3000 m on the 28th of January 2019. The multiple green lines show the different BSR-values belonging to the different time steps. The green line peaking around 1800 m height belongs to the last time step (TS 5).

Then growth curves according to $f = (1 - RH)^{-\gamma}$ with the corresponding optimal γ-values were created. The theoretic f-values in the growth curves as well as the

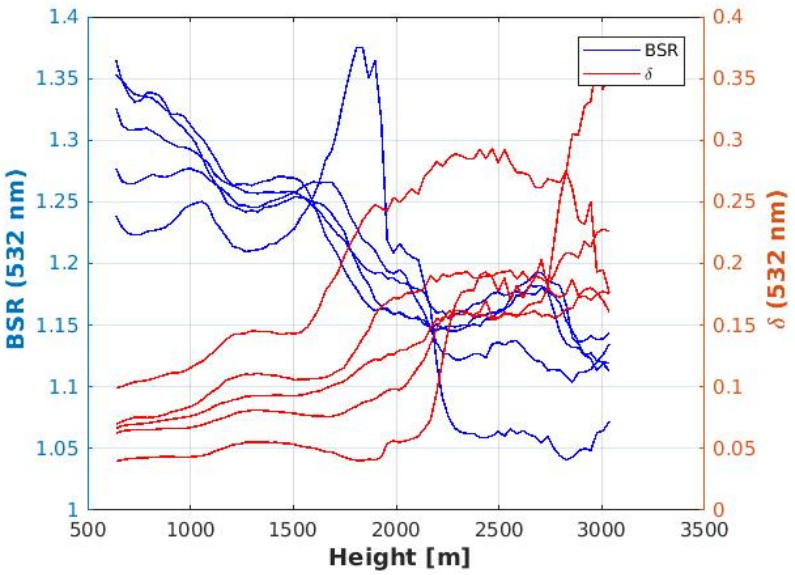

Fig. 3.23: The BSR at 532 nm (blue) and the depolarisation at 532 nm (red) plotted between a height of 600 m to 3000 m on the 28th of January 2019. The different lines in the same color indicate the different time steps. The blue line peaking around 1800 m height belongs to the last time step (TS 5).

observed β-values were then normalized. This has been done by first choosing a dry reference interval and calculating the mean f-value and the mean β-value for this interval. Subsequently, the f-values included in the growth curve were normalized by dividing those values by the dry reference f-value and the β-values were normalized by dividing through the dry reference β-value. Not for every time step the same reference values have been used, see table 3.1.

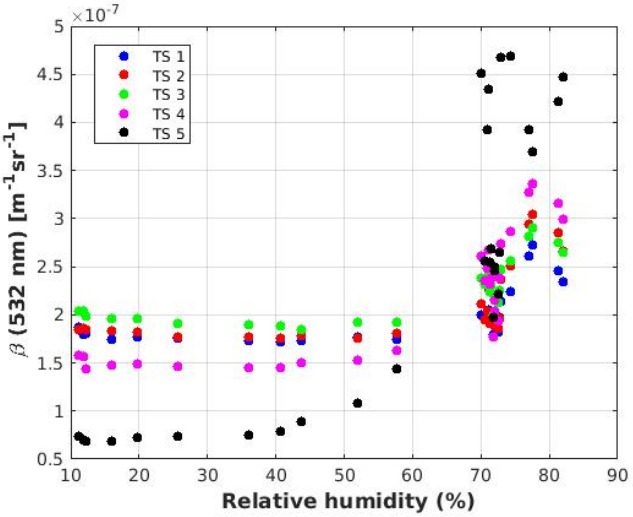

Fig. 3.24: The β (532 nm) values plotted vs. the relative humidity. The different colors indicate different time steps. Blue = 1; red = 2; green = 3; magenta = 4; black = 5.

Tab. 3.1: Gamma values and normalization characteristics of the growth curves of the time steps on the 28th of January, 2019.

Time step	γ	dry reference interval	β_{dry} (in m^{-1} sr^{-1} * 10^{-7})	f_{dry}
1	0,30	43-55%	1,75	1,22
2	0,35	43-55%	1,77	1,26
3	0,35	43-55%	1,89	1,53
4	0,65	35-45%	1,47	1,40
5	1,40	25-35%	0,736	1,51
mean	0,50	50 -60%	1,76	1,49

The growth curves of the first three time steps (respectively blue, red and green, see figure 3.25) were plotted from a RH of 55% on wards. The fourth and fifth time steps indicate a growth starting at lower relative humidity values. The fourth time step has been plotted from a RH of >50%, the fifth time step from a RH of > 40 %. Table 3.1 shows the found γ-values and the dry reference intervals for the different time steps.

No clear, single value of gamma could be determined for the growth curves of this single day, since the variability between the time steps is large. Especially the last time step (in black) differs strongly from the rest of the data. It needs to be stated that assuming the presence of hygroscopic growth includes one other, large assumption, namely that the aerosol in the considered height interval is the same and that the difference in size over this height interval is due to a change in the RH and not because it is another aerosol from another air mass.

One could go one step further by assuming the difference in backscatter of the aerosols in between the different time steps is due to the noise of the Lidar and/or due to fluctuations in the amount of the same type of aerosol (and not because of the presence of different types of aerosols on the different time points). By making this assumption, the β-values over the time steps can be averaged and a new, single growth curve (with a corresponding single γ-value) can be calculated. This has been done, however the last time step (in black, see figure 3.24) has been left out, since this one was the strongest deviating from the rest. The corresponding β-values and the fitting growth curve are shown in figure 3.26 and the growth curve shows a γ-value of 0.5. This curve does not fit so well, due to the steep increase in backscattering around 70 %. Another way to calculate the average γ-value is to average directly the γ-values from the different time steps. In this case, an average γ-value of 0.4 was calculated (again excluding time step 5).

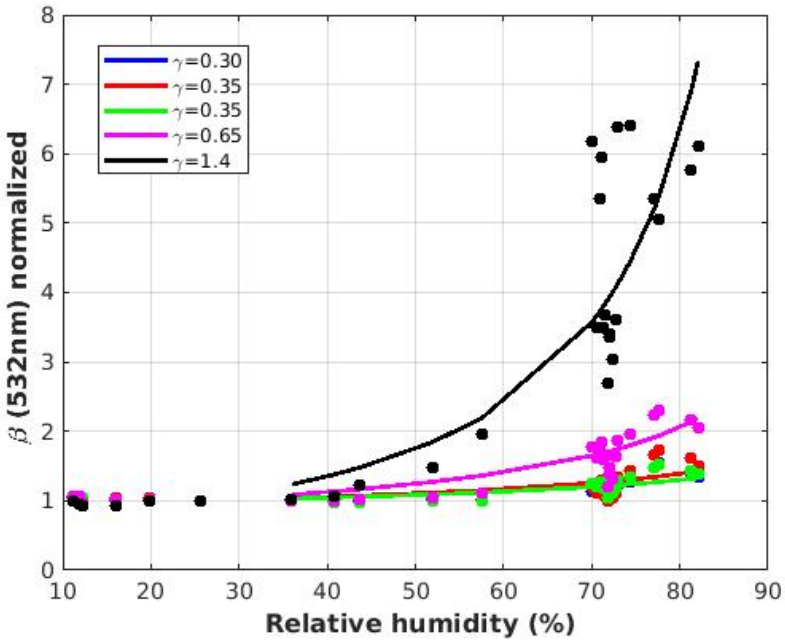

Fig. 3.25: The normalized β (532 nm) values plotted vs. the relative humidity. The different colors indicate different time steps. Blue = 1; red = 2; green = 3; magenta = 4; black = 5. For each time step, a growth curve f has been plotted. The legend indicates the corresponding optimal gamma values that are used to calculate the growth curves.

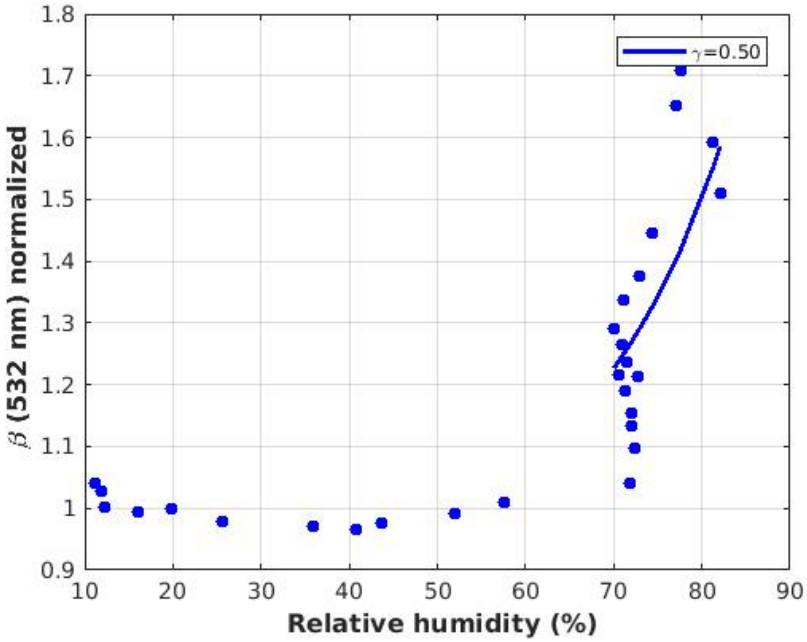

Fig. 3.26: The normalized and averaged β (532 nm) values plotted vs. the relative humidity. The legend indicates the corresponding optimal gamma value that is used to calculate the growth curve. The dots indicate the average β (532 nm) values over the first 4 time steps and the line indicates the best fitting growth curve.

Hygroscopic growth based on *in situ* data

Based on *in situ* data from the Gruvebadet observatory, hygroscopic growth for the 28th of January has been calculated using the ZSR-relationship as mentioned in section 1.5. Four components have been considered for the calculation: sea salt, ammonium sulfate, organics and an insoluble part of the captured chemistry. Its percentual molar proportions were respectively 0.692, 0.085, 0.002 and 0.220. No relative humidity measurements directly from Gruvebadet were available, but the relative humidity measured by the AWIPEV radiosonde at a height of 30 m on the 28th of January has been taken as a reference. This had a value of 60%. Using the ZSR-relationship (transforming the molar ratios to volume ratios and using this proportion to weigh the given growth factors of the components, see section 1.5), the overall growth factor was calculated. This resulting value was $GF(RH = 60\%) = 1.57$ and indicates the increase of the particle diameter at a RH of 60% compared as in a dry environment. The scattering enhancement factor $f(RH)$ was calculated using the ZSR-relationship as well and resulted in a value of $f(RH) = 2.458$. Using $f = (1 - RH)^{-\gamma}$, a gamma-value of 0.98 would be corresponding. Based on the different γ-values calculated by plotting the growth curves through the Lidar data, the following f-values at a RH of 69% are corresponding: TS 1 + TS 2: $f_{\gamma=0.3}$ = 1.31; TS 3: $f_{\gamma=0.35}$ = 1.38; TS 4: $f_{\gamma=0.65}$ = 1.81; TS 5: $f_{\gamma=1.4}$ = 3.60; Average: $f_{\gamma=0.5}$ = 1.58. In this case, the γ-values (Lidar data based) of TS 4 and TS 5 are the closest related to the f-value based on the *in situ* measurements.

Further time steps

Because the fifth time step differs strongly from time step one to four, the $\pm$ 30 min time frame around the launch of the radiosonde has been exceeded in order to study the backscatter of two more time steps (called time steps 6 and 7). Those time steps have been measured 40 respectively 50 min after launch of the radiosonde. Therefore during this time, the chance that the relative humidity changed is elevated. However, the backscatter and water vapor mixing volume ratios of those further time steps have been studied in order to see whether the observed hygroscopic growth of time step 5 continues in further time steps and whether it might be due to an increased humidity.

First, the backscatter of time steps one to seven have been plotted logarithmic against the height (see figure 3.27). Time step 4 is shown as the upper blue dotted line. Time step 5 is here extra shown in red and was the last time step being considered in the hygroscopic growth calculations. Time step 6 and 7 (respectively in green and black) show clearly higher backscatter values and the backscatter values of time

step 7 are partially larger than 2 $Mm^{-1}sr^{-1}$, indicating cloud formation. The water vapor volume mixing ratio together with the RH over height have been studied too (see figure 3.28). There is a large observed difference between the mixing ratio of time step 1 to 3 and the mixing ratios of time step 4 to 7 (which are all similar). The course of the relative humidity matches better the course of the mixing ratios of time step 4 to 7 than the mixing ratios of time step 1 to 3.

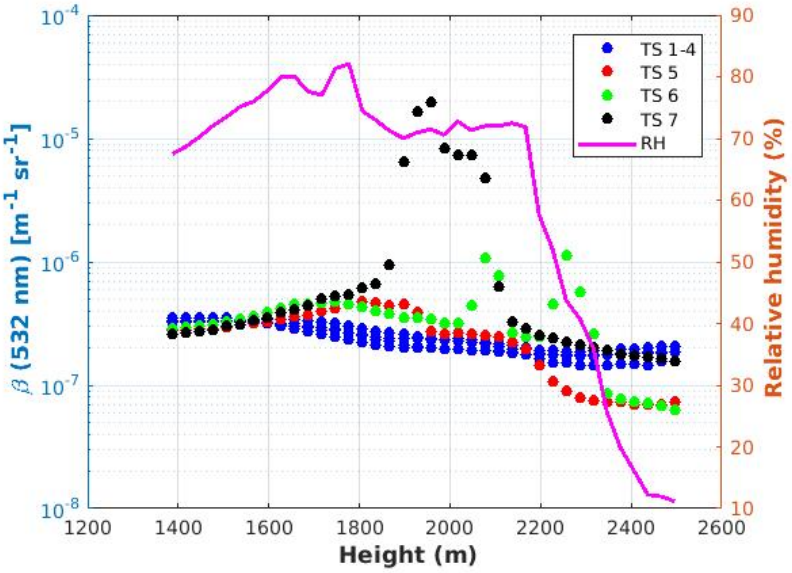

Fig. 3.27: The backscatter of time step 1 to 7 (left logarithmic y-axis) and the relative humidity (right y-axis) over height. Time steps 1 to 4 are indicated in blue, time step 5 in red, time step 6 in green and time step 7 in black. The relative humidity is indicated in magenta.

The strong increase in backscatter for time step 5 to 7 happens in the same height as where the difference between the volume mixing ratios of the time steps is the largest. A possible time dependency of the hygroscopic growth can be observed. Although time step 4 to 7 have similar volume mixing ratios (assuming similar relative humidities as well), the increase in backscatter differs between times step 4 and 7. This might indicate a temporal dependency of the hygroscopic growth. Based on the change of humidity between time step 1 and time step 4 to 7, it is actually difficult to compare the calculated hygroscopic growth factors from time step 1 to 5. Further details will be discussed in the discussion.

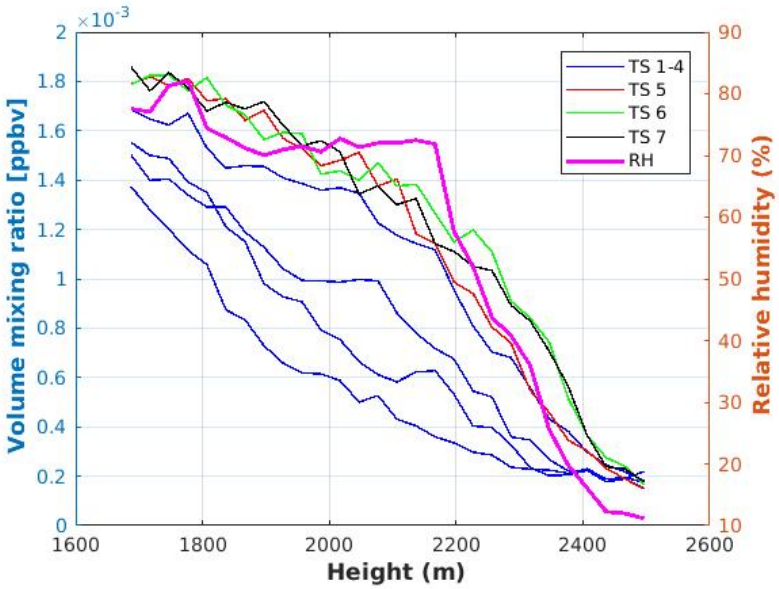

Fig. 3.28: The water vapor volume mixing ratios of time step 1 to 7 (left y-axis) and the relative humidity (right y-axis) over height. Time step 1 to 4 are indicated in blue, where the upper graph is time step 4 and the lower is time step 1. Time step 5 is indicated in red, time step 6 in green and time step 7 in black. The relative humidity is indicated in magenta.

3.3.2 Hygroscopic growth on the 6th of February, 2019

On the 6th of February, the radiosonde (launched at 10:50h that day) measured a gradient in relative humidity between 1650 to 2100 m. A contour plot with the BSR from that day over height is shown in figure 3.29. The studied time- and height span has been indicated with the red rectangle.

Just as done for the 28th of January, the RH, the BSR at 532 nm and the depolarisation ratio at 532 nm have been plotted over the height (see figure 3.30 and 3.31. A similar trend as seen on the 28th of January is visible on the 6th of February: The RH (over water and ice) and the BSR show a positive correlation, whereas the BSR and the depolarisation ratio show a negative correlation.

Since, the depolarisation ratio shows low values of close to 0% indicating no ice particles, only the relative humidity over water was considered to look for hygroscopic growth. β-values were plotted against the relative humidity. Hygroscopic growth was observed (see figure 3.32) and growth curves according to Zieger et al. (2010) were plotted for the four different time steps (figure 3.33). The growth curves were plotted from an RH of 65% on and were normalized by the mean β-value between an RH of 50% and 65%. A decrease in gamma values was observed over the time steps.

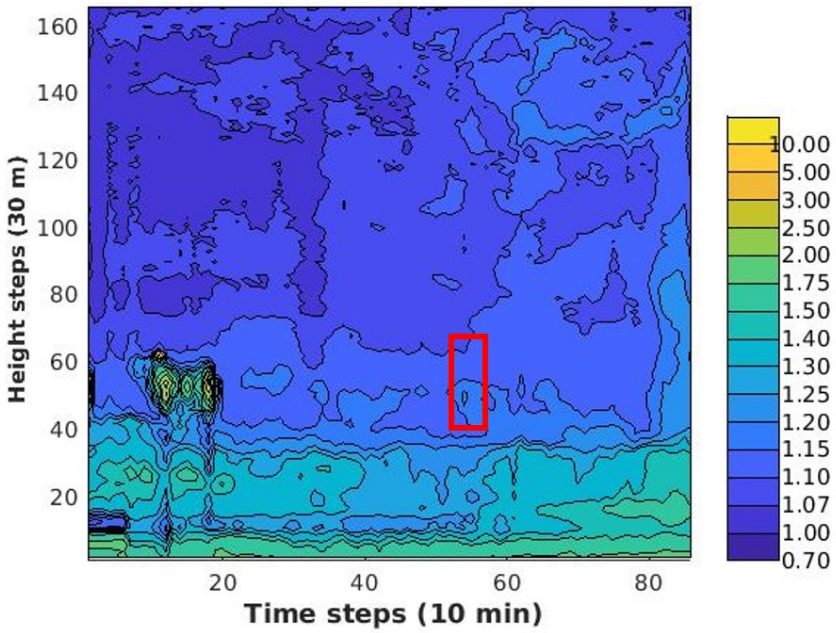

Fig. 3.29: A contour plot of the BSR belonging to the 6th of February. The x-axis represents the time steps, starting at 00:11 and ending at 16:45h. The y-axis represents the height steps starting a 0 m, ending at 5015 m. The red frame represents the time- and height frame of this case study.

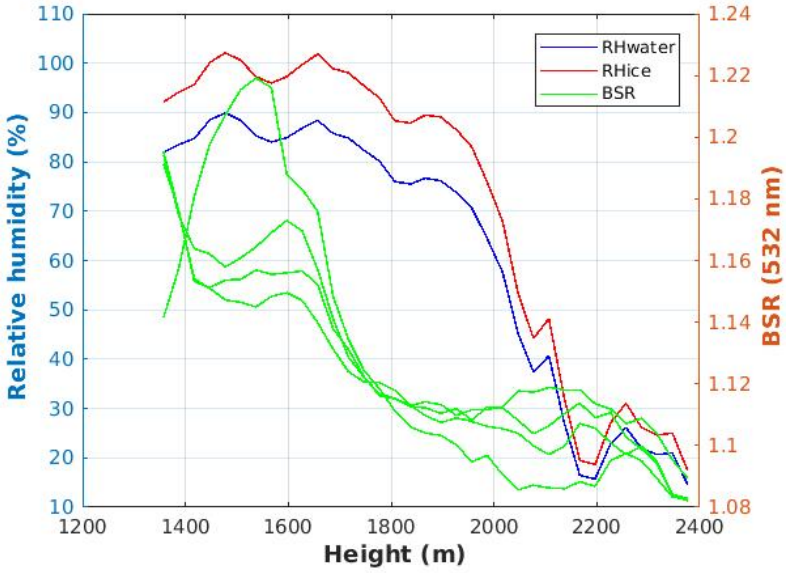

Fig. 3.30: The relative humidity profiles over water and ice (respectively blue and red) and the BSR at 532 nm (in green) between a height of 1400 to 2400 m.

Similar as for the 28th of January, a γ-value based on the mean of the time steps was created, as shown in figure 3.34, yielding a γ-value of 0.40. The average γ-value based on the mean of the calculated γ-values per time step was 0.41. Table 3.2 shows the γ-values, the normalization interval, the dry reference value for β and the

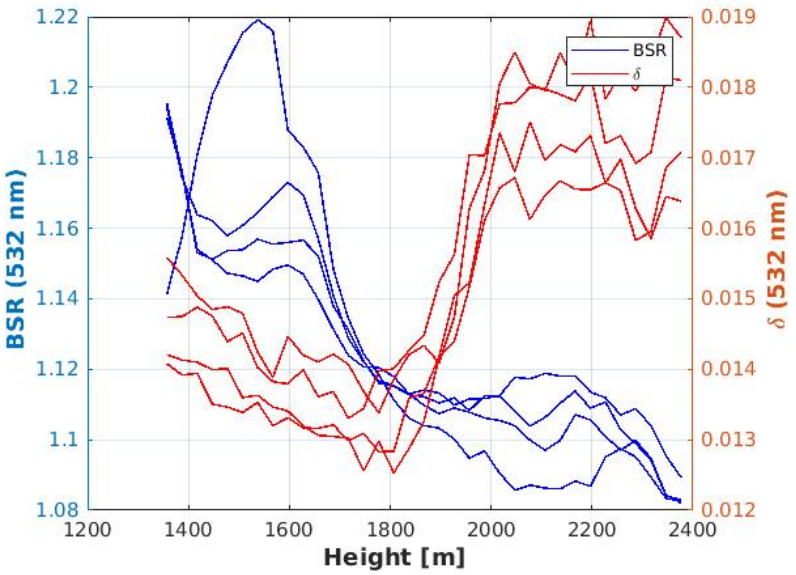

Fig. 3.31: The BSR at 532 nm (in blue) and the depolarisation ratio at 532 nm (in red) plotted between a height of 1400 to 2400 m.

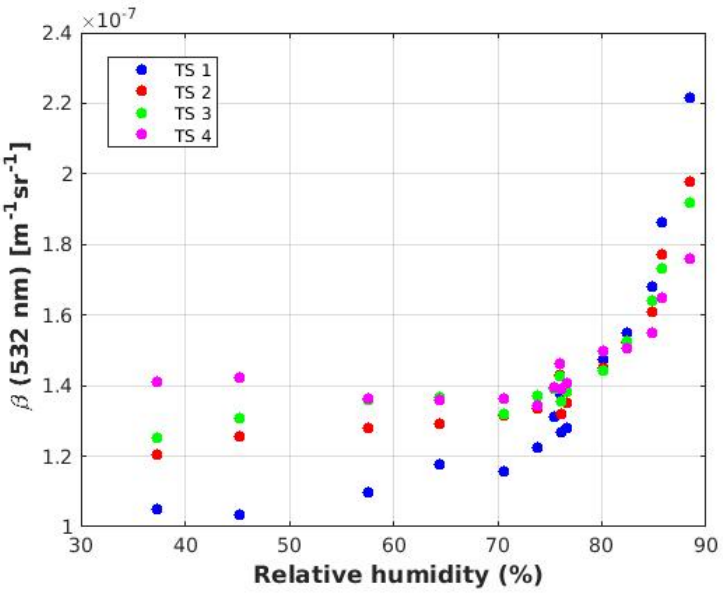

Fig. 3.32: The β (532 nm) values plotted vs. the relative humidity. The different colors indicate different time steps. Blue = 1; red = 2; green = 3; magenta = 4.

dry reference value for f for the separate time steps as well for the mean of the 6th of February.

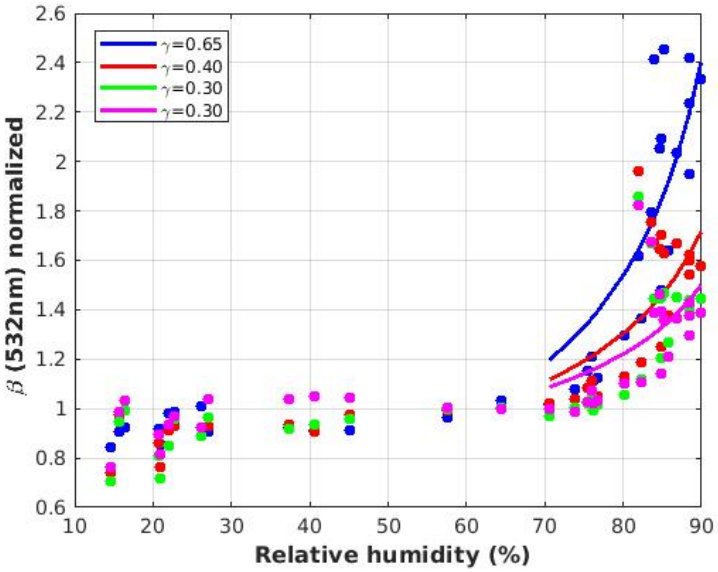

Fig. 3.33: The β (532 nm) values plotted against the relative humidity. The different colors indicate different time steps. Blue = 1; red = 2; green = 3; magenta = 4. For each time step, a growth curve f has been plotted. The legend indicates the corresponding optimal gamma value that is used to calculate the growth curves.

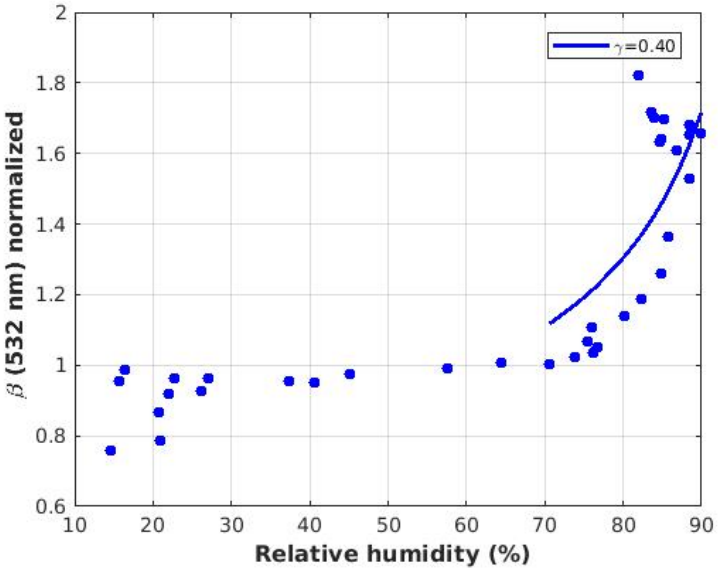

Fig. 3.34: The β (532 nm) values plotted against the relative humidity. The legend indicates the corresponding optimal γ-value that is used to calculate the growth curve. The dots indicate the average β (532 nm) values over the time steps and the line indicates the best fitting growth curve.

Tab. 3.2: Gamma values and normalization characteristics of the growth curves of the time steps on the 6th of February, 2019.

Time step	$gamma$	dry reference interval	β_{dry} (in m^{-1} sr^{-1})	f_{dry}
1	0,65	50-65%	1,137E-07	1,852
2	0,40	50-65%	1,285E-07	1,461
3	0,30	50-65%	1,364E-07	1,328
4	0,30	50-65%	1,361E-07	1,328
mean	0,40	50-65%	1,287E-07	1,461

Hygroscopic growth based on *in situ* data

Based on *in situ* data from the station Gruvebadet, hygroscopic growth for the 6th of February has been calculated in the same manner as for the 28th of January. Also, no relative humidity measurements directly from Gruvebadet were available, but the relative humidity measured by the AWIPEV radiosonde at a height of 30 m on the 6th of February has been taken as a reference. This had a value of 70%. The resulting growth factor was $GF(RH) = 1.54$ and indicates the increase in volume of the total aerosol composition at 70% compared as in a dry environment. The scattering enhancement factor $f(RH)$ was calculated as mentioned in section 2 and resulted in a value of $f(RH) = 2.359$. Using $f = (1 - RH)^{-\gamma}$, a gamma-value of 0.73 would be corresponding. Based on the different γ-values calculated by plotting the growth curves through the backscatter data, the following f-values at a RH of 69% are corresponding: TS1: $f_{\gamma=0.65}$ = 2,19; TS2: $f_{\gamma=0.40}$ = 1.62; TS3 + TS4: $f_{\gamma=0.30}$ = 1.43; Average: $f_{\gamma=0.40}$ = 1.62. The γ-value belonging to TS1 comes closest to the γ-value based on the *in situ* data.

3.4 Case Study: the 19th of January 2019

The 19th of January was chosen as one of the case study days, since for this day different data sources were available (see table 3.3). Although the time spans are different (the Italian data is from around 11 o'clock, the AWIPEV data from around 17 o'clock), the stable conditions during the 19th January could make the results on different times comparable (as is being highlighted in the discussion).

Tab. 3.3: Available data types and their time- and height ranges for the 19th of January

Data type	Time start	Time end	Height range (m)	From
In situ (size distribution)	11:10	12:19	0-600	Mauro Mazzola
Meteorological (Mozzarella)	13:43	15:02	0-1000	Mauro Mazzola
Meteorological (radiosonde)	16:47		0-30000	AWIPEV
Lidar data	08:02	23:59	600-10000	AWIPEV

3.4.1 Hygroscopic growth between 700 and 1000 m based on data from the tethered balloon and Lidar data

Backscatter data from the Lidar and relative humidity data from the Italian weather balloon "Mozzarella" were evaluated in order to determine a correlation between those data and to study hygroscopic growth. Since Mozzarella can reach maximum heights of around 1000 m and the Lidar data becomes most accurate after 600-700 m (due to the overlap problem), an height range between 700 m and 1000 m was used to compare the data from both Mozzarella and the Lidar. On the 19th of January 2019, Mozzarella ascended and descended two times, but in this analysis only the first flight is being considered (the second flight gave false results, see section 2). A gradient in the relative humidity between 700 and 1000 m was measured by Mozzarella during its first flight (see figure 3.35). The ascent between 698 m and 968 m took place from 14:16h to 14:27h, the descent from 968 m back to 698 m from 14:28h to 14:37h.

The relative humidity between 698 m and 968 m was averaged over the ascent and descent and plotted against Lidar data ± 30 min from 14:27h (see figure 3.36). An increase of the backscattering at 532 nm over the relative humidity is seen, however no clear hygroscopic growth can be derived from those data.

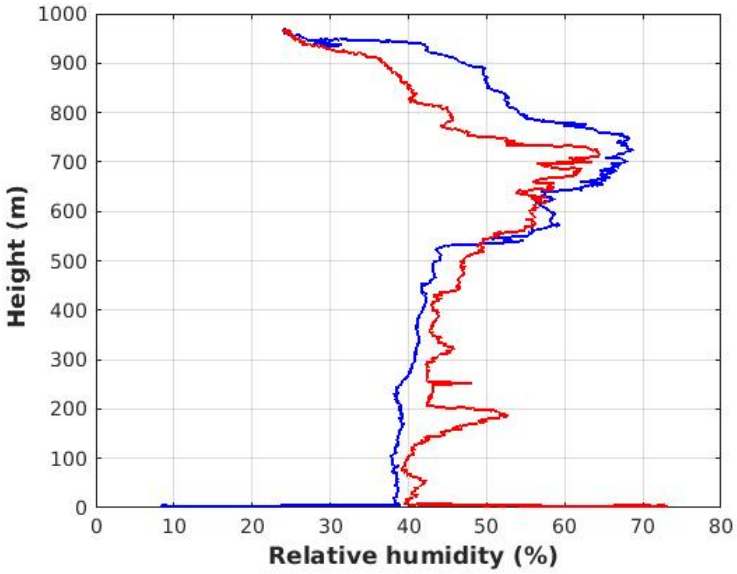

Fig. 3.35: The relative humidity profile on the 19th of January 2019 between 13:43 and 15:02h measured by the Italian weather balloon "Mozzarella". The blue graph shows the ascent of the balloon, the red graph the descent.

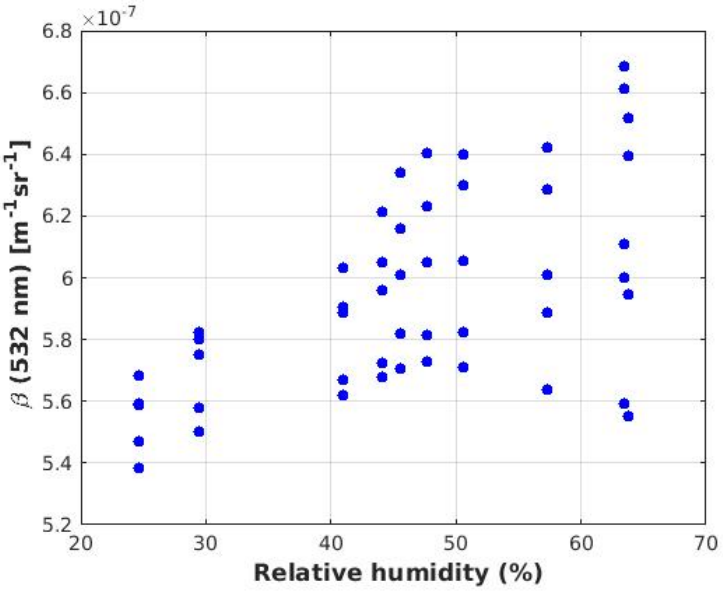

Fig. 3.36: The relative humidity vs the backscatter data over an height of 698m and 968m during the first flight of Mozzarella on the 19th of January, 2019.

3.4.2 Hygroscopic growth based on radiosonde and Lidar data

The radiosonde data showed a gradient in relative humidity (over water and ice) between a height of 700 and 1500m around 17h. The decrease of the relative humidity was correlated with a decrease in aerosol backscatter, however did not show a hygroscopic growth pattern (not shown). The decrease in backscatter was paired with an increase in depolarized light, however the depolarisation ratio was over the whole height low, indicating spherical particles (see figure 3.37).

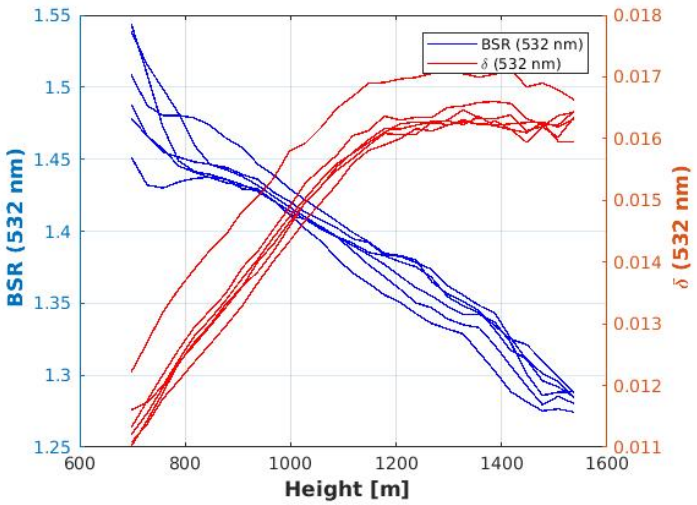

Fig. 3.37: The backscatter ratio at 532 nm (blue) and the depolarisation (red) between a height of 700 m and 1500 m on the 19th of January, 2019.

Due to the lack of a hygroscopic growth pattern, no growth curves were made.

3.4.3 Analysis of the size distribution from in situ data over a height of 0-600 m

In situ data from the research group of Mauro Mazzola (CNR Bologna) showed the size distribution of aerosols over a height of 0-600 m as seen in figure 3.38. To compare the size distribution of the different heights, the particle frequency per bin was averaged for all values from 0-100 m, from 100-300 m and from 300-600 m. The resulting three averaged size distributions are shown in figure 3.39.

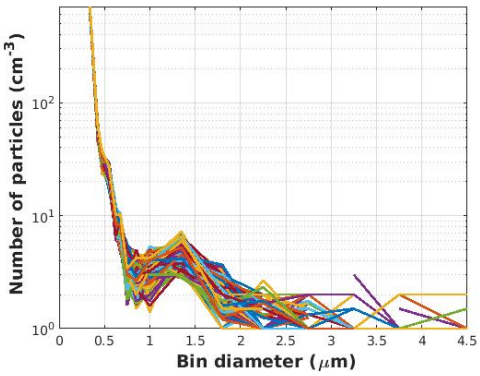

Fig. 3.38: The in situ size distribution over a height 0-600 m

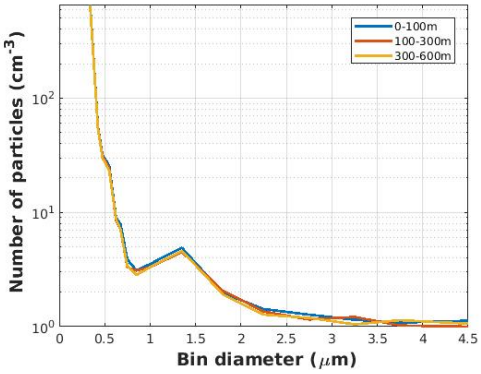

Fig. 3.39: The in situ size distribution average over 0-100 m (blue), 100-300 m (red) and 300-600 m (yellow)

This *in situ* size distribution indicates a large amount of small particles around a diameter of 0.5 μm , however smaller particles are not being captured with this technique. It looks as if only the "tail" of the size distribution has been captured and it is likely that smaller aerosol particles (between 1 and 500 nm) were present. This is indeed the case when looking at a graph of Mazzola (see figure 3.40). Between 0 and 600 m height, average concentration of 250-300 particles per cm^3 were observed. Also no difference between 0 and 600 m height was visible, indicating a homogenous aerosol distribution over this height as well as the absence of hygroscopic growth. Radiosonde data from this day (launched on 16:47h, thus more than 5 hours after the *in situ* measurements), show though a slight gradient in relative humidity (49% at 100 m, 52% at 300 m and 74% at 600 m).

Overall, no hygroscopic growth could be determined on the 19th of January. It was however observed, that from 0-600 m, mostly fine aerosols ($<$ 500 nm) were present. Also, between 600 and 1200 m, smaller sized particles were present, although this slightly decreased from 800 m on (see figure 3.40). Between 700 and 1500 m, the relative humidity decreased and slightly correlated with a decrease in backscatter,

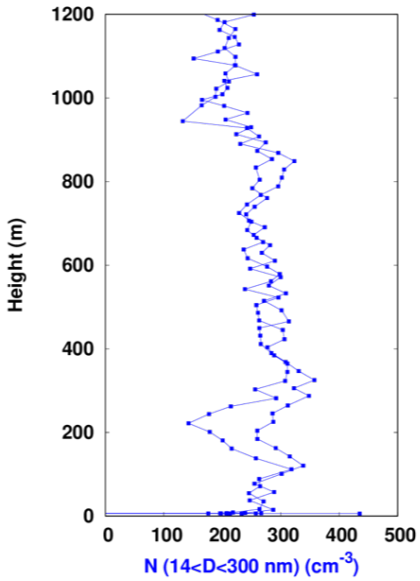

Fig. 3.40: The number of nanoparticles (between 14 and 300 nm, x-axis) over the height (y-axis) for the 19th of January. Figure taken from Mauro Mazzola without any adjustments.

however not clearly. There was a clear change in backscatter over height and a clear negative correlation with the depolarisation, however the depolarisation values were overall low, so that no significant change in the spherical shape of the aerosols can be assumed. Considering those low depolarisation values (between 1.1 and 1.6%), it is likely that the present aerosols were more spherical-like sulphate and ammonium particles.

4 Discussion

4.1 Comparing the optical aerosol properties

The observed β^{aer}-values in January to April between 700 and 1500 m were peaking around 0.4*10 $^{-6}$ m^{-1} sr^{-1}, ranging up to values of 1*10 $^{-6}$ m^{-1} sr^{-1}. The aerosol backscatter decreased over height. As stated in section 1.4.2, previous research on optical properties of aerosols has been performed and can be compared with the results of this study.

Results of the iAREA campaign in April 2014 showed most backscatter values around 0.4*10 $^{-6}$ m^{-1} sr^{-1} for the height 1000-1500 m. It is similar to the month April of this study between 700 and 1500 m, since a peak around 0.4*10 $^{-6}$ m^{-1} sr^{-1} was seen too. In the altitude 2500-5000 m in the iAREA campaign, backscatter values were peaking at 0.15*10 $^{-6}$ m^{-1} sr^{-1} and for most of the time, backscatter values no higher than 0.4*10 $^{-6}$ m^{-1} sr^{-1} were observed (with the exception of a 5 days period in which the maximum backscatter values reached up to 0.5*10 $^{-6}$ m^{-1} sr^{-1}). In this study, the backscatter peak between 3000 and 5000 m in April was around 0.15-0.20*10 $^{-6}$ m^{-1} sr^{-1}, showing similar values as measured during the iAREA campaign. The depolarisation ratio in April 2014 in the height 1000-1500 m was peaking between 0.02 and 0.03 and peaking at 0.03 between 2500 and 5000 m. In April 2019 the depolarisation ratio in the height interval 700 - 1500 m was peaking at 0.01-0.02 and the peak shifted between 1500 and 3000 m to 0.02. The color ratio has not been compared, since another scale for the color ratio has been used in the iAREA campaign. Based on those height comparisons, the patterns of the aerosol backscatter in the iAREA study appear to be similar for this study. However, in this study the depolarisation ratio appears to be lower, indicating more spherical particles in April 2019 compared to April 2014.

Shibata et al. (2018) measured typical aerosol backscatter values from January to June (from 2014 to 2018) in the first 2 km of the atmosphere around 0.4*10^{-6} m^{-1} sr^{-1}, in February and March reaching values up to 0.7*10^{-6} m^{-1} sr^{-1}. The peak around 0.4*10^{-6} m^{-1} sr^{-1} is similar in this study (although observed between January-April, only in 2019) and slightly elevated backscatter values were observed in February too (between 700 and 1500 m). However, no clear haze season as seen in the study of Shibata et al. was observed.

The master thesis of Janka (2019) highlights aerosol properties from the 1st to the 13th of March 2018 and analyzed the properties with the same height intervals as done in this study (700-1500 m, 1500-3000 m, 3000-5000 m, and 5000-10000 m). Those heights have been compared with the data for March of this study and similar trends were observed. An overview of the relative frequencies for the backscatter is seen in table 4.1. Although the height intervals are the same, the time intervals differ: Janka considered the 1st to the 13th of March 2018, whereas in this study different days throughout the full month of March were considered.

Tab. 4.1: Comparing the aerosol backscatter data of Janka (2018) of the 1st - 13th of March 2018 with the data from this study, considering the full month of March in 2019. The first value in each cell (in *italic*) represent the data of Janka (2018), the second value represents the data found in this study. Note the fact that the values of this study do not sum up as 100%: this is because the data were filtered for clouds and those values have been left out in the table and graphs, but have been included while calculating the relative frequencies.

β **(532 nm)** **(*10^{-6} m^{-1} sr^{-1})**	**700-1500 m**	**1500-3000 m**	**3000-5000 m**	**5000-10000 m**
0 - 0.1	*4.30* 4.12	*5.09* 6.47	*11.29* 30.16	*83.39* 71.34
0.1-0.2	*0.96* 10.99	*11.11* 41.30	*67.28* 50.83	*8.27* 6.98
0.2-0.3	*28.31* 25.01	*65.42* 34.67	*18.30* 7.42	*2.33* 0.71
0.3-0.4	*37.27* 30.07	*12.04* 8.81	*0.70* 2.45	*1.23* 0.18
0.4-0.5	*14.17* 12.36	*1.46* 0.45	*0.30* 1.26	*0.82* 0.14
0.5-0.6	*14.98* 1.64	*4.88* 0.19	*1.58* 0.62	*3.96* 0.04

Similar backscatter patterns for 2019 have been found as in 2014. However for 2019, lower backscatter values between 1500 and 3000 m were observed. The Arctic haze phenomenon is usually being observed below 3000 m and the lower backscatter values in 2019 indicate the absence of a clear haze season. As stated in the caption of the table, the relative frequencies of the data of this study do not sum up as 100%. This is because the cloud-filtered data have been taken into account while calculating the relative frequencies, but are not shown (neither in this table nor in the graphs as shown in section 3.1) since their backscatter values exceed 2*10^{-6} m^{-1} sr^{-1} and show cloud particles.

Also, the color ratios of the two studies have been compared (see table 4.2). However, Janka (2018) started the CR of a value of 1 whereas in this study it starts at two, due to the cloud filter, making it difficult to properly compare the data. The height intervals 3000 - 5000 m and 5000 - 10000 m have not been considered. It can be seen, that between a height of 700 and 3000 m, higher relative frequencies between

a CR of 2 and 3 were observed in March 2019 than in March 2018, whereas higher CR-values were more prevalent in March 2018, indicating larger particles in March 2019 for this height.

Tab. 4.2: Comparing the CR-values of Janka (2018) of the 1st - 13th of March 2018 with the data from this study, considering the full month of March in 2019. The first value in each cell (in *italic*) represent the data of Janka (2018), the second value represents the data found in this study. Note the fact that the values of this study do not sum up as 100%: this is because the data were filtered for clouds and those values have been left out, but have been included while calculating the relative frequencies.

CR	700-1500 m	1500-3000 m
1 - 2	*10.46*	*3.75*
2 - 3	*15.44* 44.98	*7.75* 19.31
3 - 4	*30.66* 24.06	*26.98* 32.26
4 - 5	*41.92* 7.04	*60.65* 18.32

Lastly, the depolarisation ratio has been compared with the data of Janka (see table 4.3). It is seen that between 700 to 1500 m both March 2018 and March 2019 show the highest relative frequency of 0 - 1%, indicating the presence of spherical-like particles. Between 1500 and 3000 m, both years shows most aerosols with a depolarisation ratio of 1.0 and 1.4 (2018) and 1.0 and 1.5 (2019), however for March 2019, relatively higher depolarisation ratios are observed, indicating less spherical particles. This might indicate the presence of sea salt or crustal particles in this height. Between 3000 and 5000 m, both years show the highest prevalence of aerosols with an depolarisation ratio between 1% and 2%. Between 5000 and 10000 m, March 2018 shows higher depolarisation ratios than March 2019. In this height, it is likely that those higher values come from icy particles, which might be an indication for a colder free troposphere in March 2018 than in March 2019.

Overall, March 2018 and March 2019 show similar trends in the optical properties of the aerosols. However, small differences can be observed. March 2018 shows slightly higher backscatter values from 700 tot 3000 m. Also, March 2018 shows relatively large values for the CR for this height interval compared to March 2019. Since this indicates the presence of small particles, it looks like the higher backscatter values in March 2018 are due to a larger number of particles and are not due to larger particles. The depolarisation values between March 2018 were also relatively lower than in March 2019. Overall, this shows the presence of more, smaller and rounder particles in March 2018 than in March 2019, which might indicate a higher presence of round ammonium sulfate particles (eventually combined with relatively lower amount of sea salt or crustal sources).

Tab. 4.3: Comparing the depolarisation ratios of Janka (2018) of the 1st - 13th of March 2018 with the data from this study, considering the full month of March in 2019. The first value in each cell represent the data of Janka (2018), the second value represents the data found in this study. The second and the third range differed slightly in the study of Janka compared to this study.

Range	700-1500 m	1500-3000 m	3000-5000 m	5000-10000 m
0-1.0	*50.25*	*33.83*	*8.30*	*5.76*
	35.62	8.15	11.45	11.90
1.0-1.4	*42.48*	*54.55*	*30.28*	*9.12*
1.0-1.5	23.49	32.93	26.73	21.25
1.4-2.0	*2.05*	*6.00*	*39.58*	*17.83*
1.5-2.0	13.08	26.52	26.19	22.82
2.0-2.5	*0.96*	*0.58*	*14.08*	*22.79*
	5.65	12.06	11.66	11.91
2.5-3.0	*0.63*	*0.58*	*4.67*	*20.57*
	0.93	2.92	5.99	5.15
3.0-3.5	*0.91*	*0.33*	*0.54*	*10.78*
	0.42	1.15	2.76	2.48
3.5-4.0	*0.58*	*0.24*	*0.07*	*4.13*
	0.29	0.63	1.19	1.15
4.0-5.0	*0.10*	*0.61*	*0.26*	*3.51*
	0.54	0.81	1.28	1.02

To get an impression of the different air masses having reached Ny-Ålesund at March 2018 and March 2019, the HYSPLIT trajectory model (https://www.ready.noaa.gov/HYSPLIT.php) has been used. For March 2018, 72h-backward trajectories (ending at the observatory in Ny-Ålesund at 1000 m height) in a frequency of 6 hours over the period from the 1st to the 13th of March have been been calculated (see figure 4.1). The image shows the trajectories passing through one grid squared (0.25 x 0.25 degrees) divided by the total number of trajectories (and this all times hundred to get percentages). The same has been done for March 2019, however over the period of the 1st to the 31th of March (see figure 4.2) .

It can be seen that in the first half of March 2018, all trajectories come from directly around Spitsbergen, from further north, from Greenland or from Siberia. Looking at the trajectory frequency of March 2019, it is seen that many trajectories come from directly north/north west of Spitsbergen or from the south (direction of Europe). It was thought that maybe all trajectories in March 2018 would come over land and-or sea ice, since sea-ice is usually present north of Spitsbergen, whereas in March 2019 more trajectories come from further over the open sea. This could explain the difference in observed aerosol types and the higher depolarisation ratio in March 2019, since sea salt is -based on the trajectories- likely to be a more present aerosol. However, figure 4.3 shows the absence of direct sea-ice north of Spitsbergen in March 2018, thus this does not directly support this theory. It also does not exclude it, because the trajectory endpoints show the sources of the trajectories 3 days ago.

It can still be that in March 2018, most trajectories came over sea-ice further north, whereas in March 2019 more trajectories came from more southern latitudes. It needs to be stated though, that trajectory analysis for polar regions is generally tricky, since not a lot of meteorological data is present for its calculation. It can however give an indication of the meteorology and can serve as a completion of the atmospheric situation.

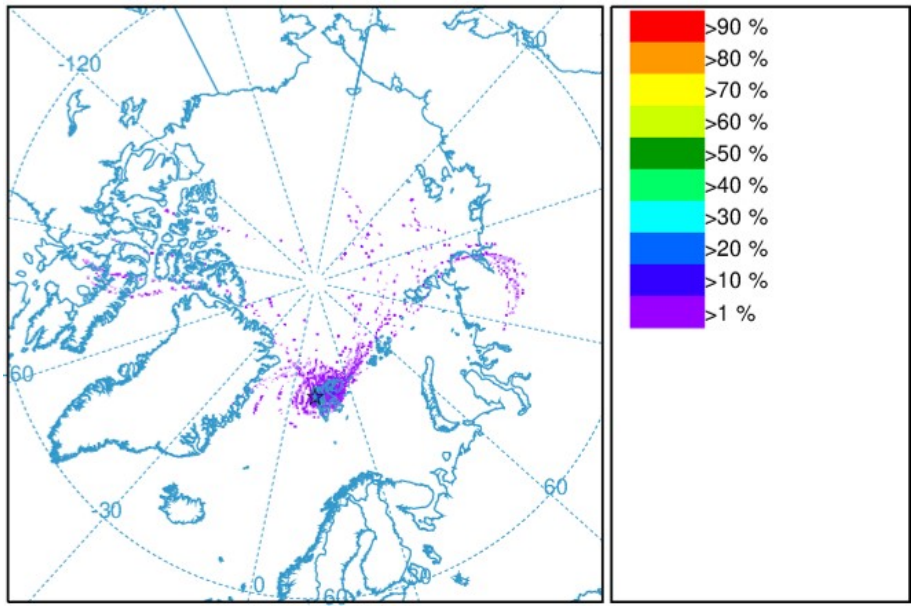

Fig. 4.1: The 72h- backward trajectory frequencies ending at the observatory in Ny-Alesund at 1000 m height for the 1st to the 13th of March 2018. The frequencies have been calculated by dividing the number of endpoints per grid squared by the total number of trajectories (times hundred).

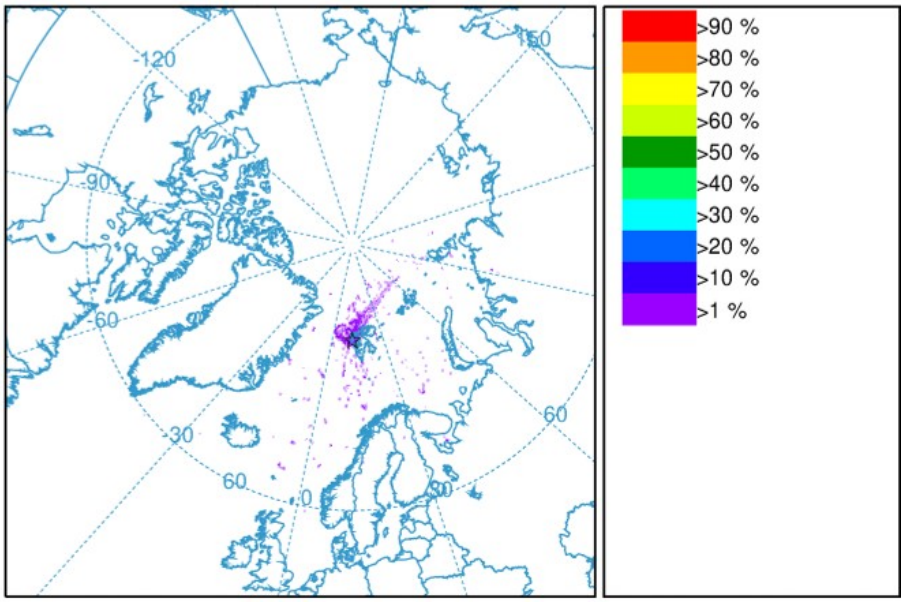

Fig. 4.2: The 72h- backward trajectory frequencies ending at the observatory in Ny-Alesund at 1000 m height for the 1st to the 31st of March 2019. The frequencies have been calculated by dividing the number of endpoints per grid squared by the total number of trajectories (times hundred).

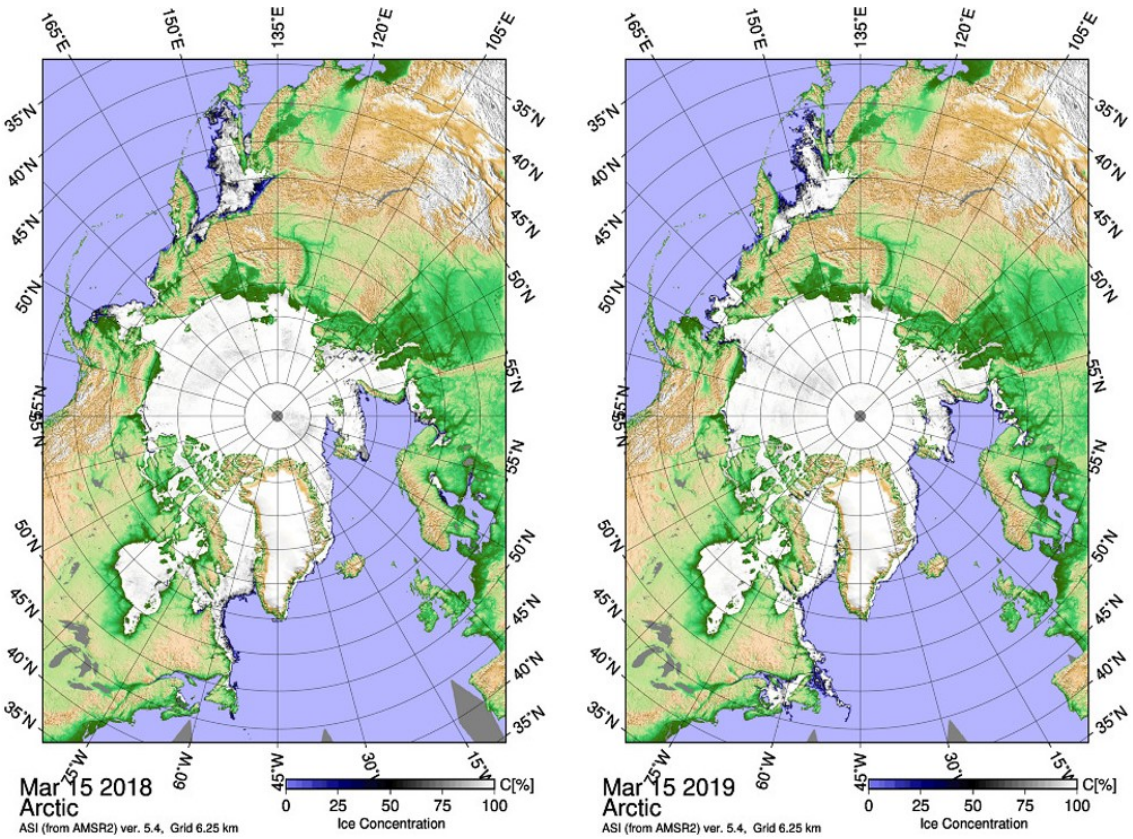

Fig. 4.3: Sea-ice conditions on the 15th of March 2018 (left) and 2019 (right). Data obtaines from "Meereisportal" (Grosfeld et al., 2016).

4.2 Comparing the observed hygroscopic growth

One of the challenges this study poses, is the comparison of Lidar and *in situ* data to determine the hygroscopic growth. Different aspects will be discussed in this section.

4.2.1 Hygroscopic growth on the 28th of January

Based on the Lidar data, growth curves were established. As seen in the results, large differences exist between the growth curves. It is common that the aerosol backscatter values experience an error of about 10% in the Lidar data. However, the differences observed in the Lidar data are beyond that value. On the 28th of January, the backscatter values in dry conditions of time steps 1 to 3 were all between 1.8 and $2*10^{-6}$ m^{-1} sr^{-1}, of time step 4 $1.5*10^{-6}$ m^{-1} sr^{-1} and of time step 5 $0.7*10^{-6}$ m^{-1} sr^{-1}. Since time step 4 and 5 (especially time step 5) were deviating strongly from time step 1 to 3, this difference was unlikely to be simply caused by noise and was likely to have another reason. It could have been another aerosol, but since the aerosol composition in the Arctic winter is stable and homogeneous and unlikely

to change quickly, this was considered unlikely. A change in humidity was thought to be more likely. For this reason, the water vapor mixing ratios of time step 1 to 7 were plotted. It was observed that the mixing ratios deviated strongly from each other. The measured relative humidity fitted better the mixing ratios of time step 4 to 7 as the mixing ratios from time step 1 to 3. This can be explained by the fact that time step 1 to 3 were measured before the launch of the radiosonde and time step 4 and 5 after the launch. Apparently, over this time the volume mixing ratio changed and since the relative humidity correlated well with the volume mixing ratio, it is assumed that the relative humidity changed as well.

Considering this, the hygroscopic growth calculated in time step 4 and 5 should be more accurate and precise due to the better matching relative humidity. However between time step 4 and 5, still a change in hygroscopic growth was seen ($\gamma_{TS=4}$=0.65 and $\gamma_{TS=5}$=1.4) and the backscatter for time step 6 and 7 increased further. The question is which part of the hygroscopic growth is still strongly influenced by the chemistry of the aerosol (and can therefore be used as a characteristic for aerosols) and which part is due to the further development of droplets and their processes (the adhesive influence of the water shield around the aerosol and collision of droplets). The aerosols in time step 6 and 7 are already forming cloud droplets and this growth is likely not being influenced anymore by the original CCN. Following this logic, the hygroscopic growth of time step 4 should be most typical for the observed aerosol, since these aerosols have been for the first time exposed to higher values of the relative humidity.

It was furthermore speculated that the observed increase in hygroscopic growth between time step 4 and 5 can be due to a temporal delay of hygroscopic growth (e.g. the aerosols first start growing after a few seconds/minutes). However, in this case, hygroscopic growth in time step 4 did start. It is a matter of definition whether the parameters belonging to this initial hygroscopic growth are considered typical for the aerosol or whether the parameters belonging to the later hygroscopic growth are. A study of Sjogren et al. (2007) showed that aerosols need more than 40 seconds to reach equilibrium at high RH (>85%, depending on the chemical composition). In this master study, no equilibrium is being reached without formation of a water cloud. Maybe hygroscopic growth was directly followed up by further droplet/cloud forming processes. Considering that equilibrium might be reached after 40 s, one would say that the hygroscopic growth happened in time step 4 is most realistic for the hygroscopic growth of the aerosol.

The increase in hygroscopic growth in time step 4 and 5 due to the increase in water vapor mixing ratio does not explain though the partly lower backscatter values at higher heights (between 2200 and 2400 m). It might be related to the cloud formation around 2000 m and the resulting forming turbulence (mixing the aerosols

above the cloud in the cloud). This is however just speculation and needs more substantiation.

4.2.2 Hygroscopic growth on the 6th of February

On the 6th of February, the variability between the β-value in the dry state was less than on the 28th of January, but still showed more than 10% difference. The found γ-values were less deviating as well. The *in situ* data showed a γ-value of 0.73 and comes closest to the highest modelled γ-value based on the Lidar data (which was 0.65 in the first time step).

Based on those two case studies, one would say that the hygroscopic growth calculation based on the Lidar data underestimates the γ-value belonging to the parametrized growth function $f(RH)$ or that the γ-value based on the *in situ* data overestimates the growth. However, this assumes that one of the methods give a correct estimation of the growth factor. Both methods were rather uncommon to calculate the hygroscopic growth with and the possible errors will be highlighted in the next section. One other way to estimate the correctness of the calculated γ-values is to compare those with the ones based on other research.

Zieger et al. (2010) measured $f(RH)$-, $g(RH)$- and γ-values from July to October 2008 in Ny-Ålesund using *in situ* techniques (dry- and wet nephelometers, SMPS and OPC) and Mie theory. Over this time, an average $\gamma_{>75\%}$-value of 0.58 and an $g(RH = 85\%)$ of 1.61 were observed. Janka (2018) studied hygroscopic growth in March 2018 based on Lidar data and showed average γ-values around 0.6. Based on those values, the estimated γ-values based on the *in situ* data appear to be overestimated.

4.2.3 Errors in Lidar and *in situ* data

Comparing the Lidar and the *in situ* data is not so trivial. As stated before, the Lidar data have their own systematic error. Not only generates the Lidar an error when measuring, also in the analysis of the data errors can develop. Another master student (Federica Bertuzzi, private communication) showed that the resolution of the analysis has an influence on the value of the extinction, although the RAW data does not change. This has not been shown for the backscatter or for other parameters so far, but it generally shows, that there can be more sources of errors, making comparison with other systems again harder. Calculating the $f(RH)$-values from the β-values is again a new source of errors, depending on the selection of the data and on the selection of the reference intervals.

Considering the *in situ* data, the used methods to calculate first the $GF(RH)$ and second the $f(RH)$ are not too precise neither. To calculate the $GF(RH)$ with the ZSR-relationship, only four components (sea salt, ammonium sulfate, organic components and an insoluble part) have been considered. One could go more into detail to determine more precisely the different components and their molar volumes in the air and using more specific growth factors to calculate the overall growth factor using the ZSR-relationship. There are likely also errors in measuring the components with the PM10-filter, but since this has not been conducted, no details are known about this.

Comparing the Lidar and *in situ* data as done in this study poses more (large) errors. First, there are spacial errors. The compared heights were not corresponding, since the *in situ* data were measured on the surface, although the Lidar data used to determine hygroscopic growth were measured between 1500 and 2000 m height. Additionally, the Lidar data were measured in the observatory in Ny-Ålesund, whereas the *in situ* data were measured in Gruvebadet. Also, there are temporal errors. First, the relative humidity used in the calculations was just from one time point: the time point of launching the balloon (the time difference between the launch and reaching the considered heights has been ignored). The used Lidar data are from maximum $\pm$ 30 min away from the launch of the radio sonde. Possible changes in relative humidity in this hour are not being considered. A larger temporal error forms when then comparing the *in situ* with the Lidar data. The *in situ* data are being collected over 48h, therefore just giving an impression of the aerosol composition in the air. For the 28th of January, the *in situ* data retrieved on the 28th of January have been used, actually covering data from the 27th and the 28th of January. For the 6th of February, *in situ* data covering the 5th and the 6th of February have been used.

Despite the large uncertenties of errors, it has been chosen to compare the data with each other. This is mostly since the atmosphere in the polar night is usually relatively stable. For the 28th and the 6th of February, the stability has not been checked, but a stable stratified atmosphere with a relatively homogeneous distribution of aerosols is common. Concerning the hygroscopic growth, it might be interesting to take the *in situ* data from the days following the case study (*in situ* data from the 29th and 30th for the case study of the 28th of January for example). In case of a stable troposphere, aerosol particles between 1500 and 2000 m height might reach the surface in the following days. For the 19th of January, the stability of the first kilometers has been studied.

4.3 Comparing the different data sets for the 19th of January

Although the various data sets on the 19th of January are not within the same time span of hours and seconds, it was decided that they can be used for intercomparison, based on some observations.

First, it is seen from the *in situ* data that their is barely any difference between the *in situ* size distribution between 0 m to 600 m height. This indicates a stable, inversed troposphere, typical for Arctic winter conditions. Second, the water mixing ratio from the Lidar data over a time span from 10:40h to 11:40h and the mixing ratio measured by the radiosonde at 16:47h have been compared and show no strong difference (see figure 4.4). Up to 1.5 km height, the noise of the Lidar data is small enough to consider those data. This indicates stable weather conditions during the considered time span. Third, wind Lidar data show low wind speeds, indicating a stable first 1000 m (see figure 4.5).

Based on those three observations, it was decided to consider the first 1500 m of the atmosphere between 10h and 17:30h (the relevant time span) as constant and stable, which allows to compare the different data sets.

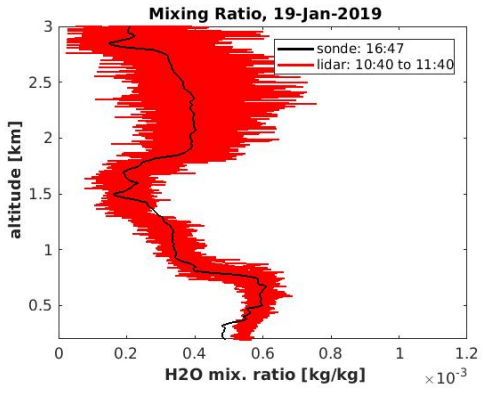

Fig. 4.4: Comparing the water mixing ratio derived from Lidar data (red) with the measured mixing ratio by the AWIPEV radiosonde.

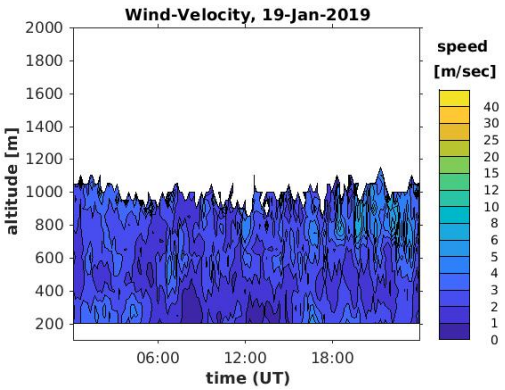

Fig. 4.5: Wind speed on the 19th of January measured by the wind Lidar at the AWIPEV station.

5 Conclusion and future work

This master thesis studied the optical aerosol properties from January to April 2019 and compared hygroscopic growth calculations based on Lidar and on *in situ* data.

5.1 Conclusion

The observed optical values were in correspondence with previous research, although due to different campaign times, could not always be compared precisely. In the lower atmosphere - between 700 and 1500 m height - typical values of β^{aer} at 532 nm were around 0.35*10^{-6} m^{-1} sr^{-1} and reached up to 1.0*10^{-6} m^{-1} sr^{-1}. The backscattering decreased with the height. For 700-1500 m, δ_{532}-values were typically between 0.1 and 0.15, whereas in other heights, the depolarisation ratio was slightly higher. The color ratio between 700 and 1500 m was mostly between 2 and 3 and increased with height. The Lidar ratio at 355 nm between 700 and 1500 m was between 0 and 50 sr, increasing for 1500-3000 nm. For higher altitudes, the LR was too noisy to determine precisely. Comparing March 2019 to March 2018, March 2019 shows lower backscatter values between 700 and 3000 m. The depolarisation values in March 2019 were higher as in March 2018. March 2019 shows therefore less particles, which are less spherical as compared to March 2018.

The found hygroscopic growth in the two case studies showed estimated γ-values of 0.98 (28th of January) and 0.73 (6th of February) based on *in situ* data. This indicates moderate to strong hygroscopic growth. The γ-values calculated based on the Lidar data showed lower values than those based on the *in situ* data. On the 28th of January, Lidar data showed γ-values between 0.3 and 1.4, however due to a change in relative humidity over the measured time, a γ-value of 0.65 is being considered the most realistic. For the 6th of February, the average calculated γ-value was 0.4. The Lidar data show large uncertainties in the calculated γ-values and growth factors. To achieve better comparison of Lidar and *in situ* data concerning hygroscopic growth, further research is needed.

5.2 Future work

Using the same data set as in this master thesis, more statistical analysis can be done on the error of the calculation of the hygroscopic growth to get more statistically profound results. Depending on the data set, different γ-values can be determined as well (for example for an RH of $> 75\%$ and $< 60\%$, as done by Zieger et al. (2010)).

There is also the possibility to analyze the composition of the aerosols based on the *in situ* data more precisely and therefore to calculate the growth factors and the gamma values more accurately.

To validate the calculation of the growth factor and the gamma values based on data from the PM10-filter, it would be interesting to compare this with growth factors and gamma values calculated in the same way as Zieger et al. (2010) has done. This would require the set up of Zieger et al. (2010) in the same height and time as the PM10 filter. Ideally this would be on Zeppelin, to decrease the influence of Ny-Ålesund on the aerosol composition.

Generally, a good temporal resolution of regular Lidar measurements and a high frequency of launched weather balloons at the AWIPEV station would offer a larger probability of finding a strong gradient in relative humidity at the same time as Lidar data would be present. This is helpful for finding more case studies to study the hygroscopic growth.

Combining remote sensing and *in situ* data can be helpful to complement and validate the data measured by the single instruments. This master thesis used the opportunity and the expertise of different people and research groups to start this collaboration and hopefully gives an impulse towards more collaboration in order to get new insights in aerosol research.

Acknowledgement

To start, I would like to thank my both supervisors, Prof. Dr. Andreas Held und Dr. Christoph Ritter for the great supervision during my thesis. I always got the feeling that you did not see me as a student who needs to be graded for her thesis, but as scientist who was performing her research. Your interest in my work and the willingness to receive any questions, supported me a lot. A special thanks to Christoph, because, well, you really explained me A LOT about the Lidar, optics and physics in general and always had time for questions. But not only did you teach me about science, you also brought my German to a next level. If there existed something like the language level "C3", your German would be it. Since writing down something is a good way to remember it, I also did this. At the end of the acknowledgment you will find a little poem inspired by your sayings :)

A fantastic experience gained during the time I wrote my thesis, was of course my four-month stay in Ny-Ålesund. A big thanks to Roland, Christoph and Greg, who initially made my stay in Ny-Ålesund possible. Thanks a lot to Marion, Holger, Peter and Wilfried for the ozone-, radiosonde- and Lidar training and support. Also, *merci* to everybody being involved in the process of making me stay longer in Ny-Ålesund and giving me work there (K/Clara, Lisa, Philipp Fischer, Roland, Greg) and as well the people who made my stay in Ny-Ålesund the way it was (especially Greg, Gwen and Christelle). This was a great opportunity and gave the Corona situation a very positive touch for me.

Thank you Daniel and Kathi for correcting the German part in this thesis (and yes, the corrections were needed) and for the many nice lunch- and coffee breaks during my thesis time at AWI.

Generally, a big thanks to everybody in the atmo-group. You are cool bunch of people and nice colleagues!

And now the "poem". It does not follow any rhyme scheme whatsoever. It is a bit "larifari".

Meine Masterarbeit mit Christoph

"Und genau das ist da,
wo der Hase im Pfeffer liegt!", meinte Christoph
"Wenn du die Analyze hinkriegst,
bist du es die den Kasus Knacktus besiegt!"

Aber die Daten waren teilweise Kraut und Rüben,
da musste ich wohl noch viel üben.
Und in meinem blassen Antlitz,
spiegelte das Bildschirm diese reine Mumpitz.

Am Anfang was vieles weder Fisch noch Fleisch,
und die Kuh war noch nicht vom Eis,
es gab noch viel zu tun,
da fehlte wohl noch viel Beweis.

Dann krallte ich mich wieder an Christophs Matlabdatei,
dessen passenden Name Faulpilz sei,
aber die Arbeit war noch nicht vorbei,
es war noch gar nicht das Gelbe vom Ei.

Aber Gutding will Weile haben,
und Hopfen und Malz waren noch nicht verloren,
Mühsam nährt sich wohl auch das Eichhörnchen,
Ich war halt nur in Ny-Ålesund eingefroren.

Und dann ann haben wir irgendwann,
nach vielen Artikeln und Büchern,
Den Kasus Knacktus und den Fehlerteufel besiegt,
Und war die Arbeit in trockenen Tücher.

Christoph, halt die Ohren steif und bis zu unserem nächsten Lazarett-Treffen!

Bibliography

(AC)^3 (2020). *Arctic Amplification: Climate Relevant Atmospheric and Surface Processes and Feedback Mechanisms*. URL: http://www.ac3-tr.de/overview/ (visited on Aug. 4, 2020) (cit. on p. 2).

Albrecht, Bruce A. (1989). „Aerosols, Cloud Microphysics, and Fractional Cloudiness“. In: *Science* 245, pp. 1227–1230 (cit. on p. 3).

Atmospheric Physics, Leibnitz Institute of (2020). *Remote Sensors*. URL: https://www.iap-kborn.de/en/research/department-optical-soundings-and-sounding-rockets/instruments-and-models/alomar-rmr-lidar/ (visited on Aug. 5, 2020) (cit. on p. 9).

Boucher, Olivier (2015). „Atmospheric Aerosols“. In: *Atmospheric Aerosols: Properties and Climate Impacts*. Dordrecht: Springer Netherlands, pp. 9–24 (cit. on p. 5).

Bozem, Heiko, Peter Hoor, Daniel Kunkel, et al. (2019). „Characterization of transport regimes and the polar dome during Arctic spring and summer using in situ aircraft measurements“. In: *Atmospheric Chemistry and Physics* 19, pp. 15049–15071 (cit. on p. 16).

DWD, Deutscher Wetterdienst (2020). *Partikel Anzahlkonzentration*. URL: https://www.dwd.de/DE/forschung/atmosphaerenbeob/zusammensetzung_atmosphaere/aerosol/inh_nav/anzahlkonzentration.html (visited on Oct. 1, 2020) (cit. on p. 16).

EEA, European Environment Agency (2017). *Arctic — why should I care?* URL: https://www.eea.europa.eu/signals/signals-2010/arctic (visited on Aug. 4, 2020) (cit. on p. 4).

Gao, Yonggang, Shing Bor Chen, and Liya E.Yu (2007). „Efflorescence relative humidity of airborne sodium chloride particles: A theoretical investigation“. In: *Atmospheric Environment* 41, pp. 2019–2023 (cit. on p. 6).

Gassó, S., D. A. Hegg, D. S. Covert, et al. (2000). „Influence of humidity on the aerosol scattering coefficient and its effect on the upwelling radiance during ACE-2“. In: *Tellus B: Chemical and Physical Meteorology* 52.2, pp. 546–567.

Goff, J. and S. Gratch (1946). „Low-pressure properties of water from -160 tot 212 F“. In: *Transactions of the American Society of Heating and Ventilating Engineers* 51, pp. 125–164 (cit. on p. 6).

Grosfeld, K., R. Treffeisen, J. Asseng, et al. (2016). „Online sea-ice knowledge and data platform <www.meereisportal.de>“. In: 85, pp. 143–155 (cit. on p. 56).

Gysel, M., E. Weingartner, S. Nyeki, et al. (2004). „Hygroscopic properties of water-soluble matter and humic-like organics in atmospheric fine aerosol“. In: *Atmospheric Chemistry and Physics* 4, pp. 35–50 (cit. on p. 19).

Hara, K., S. Yamagata, T. Yamanouchi, et al. (2003). „Mixing states of individual aerosol particles in sprinArctic troposphere during ASTAR 2000 campaign“. In: *Journal of Geophysical Research: Atmospheres* 108.

Held, A, IM Brooks, C Leck, and M Tjernstrom (2011). „On the potential contribution of open lead particle emissions to the central Arctic aerosol concentration“. In: *Atmospheric Chemistry and Physics* 11, pp. 3093–3105.

Herber, Andreas, Larry W. Thomason, Hartwig Gernandt, et al. (2002). „Continuous day and night aerosol optical depth observations in the Arctic between 1991 and 1999“. In: *Journal of Geophysical Research: Atmospheres* 107.

Hoff, R. M., W. R. Leaitch, P. Fellin, and L. A. Barrie (1983). „Mass size distributions of chemical constituents of the winter Arctic aerosol“. In: *Journal of Geophysical Research: Oceans* 88.C15, pp. 10947–10956 (cit. on p. 4).

Hoose, C. and O. Möhler (2012). „Heterogeneous ice nucleation on atmospheric aerosols: a review of results from laboratory experiments“. In: *Atmospheric Chemistry and Physics* 12.20, pp. 9817–9854 (cit. on p. 34).

Klett, James D. (1985). „Lidar inversion with variable backscatter/extinction ratios“. In: *Applied optics* 24.

Klonecki, A., P. Hess, L. Emmons, et al. (2003). „Seasonal changes in the transport of pollutants into the Arctic troposphere-model study“. In: *Journal of Geophysical Research: Atmospheres* 108 (cit. on p. 16).

Kulla, Birte Solveig and Christoph Ritter (2019). „Water Vapor Calibration: Using a Raman Lidar and Radiosoundings to Obtain Highly Resolved Water Vapor Profiles“. In: *Remote Sens* 11, p. 616 (cit. on p. 22).

Leaitch, W.R., R.M. Hoff, and J.I. MacPherson (1989). „Airborne and lidar measurements of aerosol and cloud particles in the troposphere over Alert Canada in April 1986.“ In: *Journal of Atmospheric chemistry* 9, pp. 187–211 (cit. on p. 4).

Lubin, D. and A. Vogelmann (2006). „A climatologically significant aerosol longwave indirect effect in the Arctic.“ In: *Nature* 439, pp. 453–456 (cit. on p. 3).

Mueller, Kim Janka (2019). *Characterisation of Arctic Aerosols on the basis of Lidar- and Radiosonde-Data*.

Myhre, G., D. Shindell, F.-M. Bréon, et al. (2013). „Anthropogenic and Natural Radiative Forcing“. In: *Climate Change 2013: The Physical Science Basis. Contribution of Working Group I to the Fifth Assessment Report of the Intergovernmental Panel on Climate Change*. Ed. by Stocker T.F., D. Qin, G.-K. Plattner, et al. Cambridge University Press. Chap. 8 (cit. on p. 4).

NASA, Earth Observatory (2020). *Aerosol Optical Depth*. URL: `https://earthobservatory.nasa.gov/global-maps/MODAL2_M_AER_OD` (visited on Aug. 4, 2020) (cit. on p. 7).

NASA, Earthdata (2020). *Remote Sensors*. URL: `https://earthdata.nasa.gov/learn/remote-sensors` (visited on Aug. 5, 2020) (cit. on p. 8).

NOAA, National Centers for Environmental Information (2020). *State of the Climate: Global Climate Report for May 2020*. URL: https://www.ncdc.noaa.gov/sotc/global/202005/supplemental/page-1 (visited on Sept. 27, 2020) (cit. on p. 1).

NPI, Norwegian Polar Institute (2020). *TopoSvalbard*. URL: https://toposvalbard.npolar.no/ (visited on June 11, 2020) (cit. on p. 15).

Quinn, P. K., T. L. Miller, T. S. Bates, et al. (2002). „A 3-year record of simultaneously measured aerosol chemical and optical properties at Barrow, Alaska". In: *Journal of geophysical research. Atmospheres* 107 (cit. on p. 3).

Richter-Menge, J., J. E. Overland, and J. T. Mathis (2019). *Arctic Report Card 2019* (cit. on p. 1).

Ritter, C. (2019). *Presentation: Lidar measurements of properties and dynamics of aerosol* (cit. on p. 6).

Ritter, C., R. Neuber, Alexander Schulz, et al. (2016). „2014 iAREA campaign on aerosol in Spitsbergen – Part 2: Optical properties from Raman-lidar and in-situ observations at Ny-Ålesund". In: *Atmospheric Environment* 141, pp. 1–19.

Shaw, Glenn E. (1983). „Evidence for a central Eurasian source area of Arctic haze in Alaska". In: *Nature* 299, pp. 815–818 (cit. on p. 3).

– (1995). „The Arctic Haze Phenomenon". In: *Bulletin of the American Meteorological Society* 76.12 (cit. on p. 4).

Shibata, T., K. Shiraishi, M. Shiobara, S. Iwasaki, and T. Takano (2018). „Seasonal Variations in High Arctic Free Tropospheric Aerosols Over Ny-Ålesund, Svalbard, Observed by Ground-Based Lidar". In: *Journal of Geophysical Research: Atmospheres* 123, pp. 12353–12367.

Sjogren, S., M. Gysel, E. Weingartner, et al. (2007). „Hygroscopic growth and water uptake kinetics of two-phase aerosol particles consisting of ammonium sulfate, adipic and humic acid mixtures". In: *Journal of Aerosol Science* 38.2, pp. 157–171.

Stohl, A. (2006). „Characteristics of atmospheric transport into the Arctic troposphere". In: *Journal of Geophysical Research: Atmospheres* 111 (cit. on p. 16).

Stokes, R.H. and R.A. Robinson (1966). „Interactions in aqueous nonelectrolyte solution. I. Solute-solvent equilibria." In: *Journal of Physical Chemistry* 70, pp. 2126–2130 (cit. on p. 19).

Tunved, P., J. Ström, and R. Krejci (2013). „Arctic aerosol life cycle: linking aerosol size distributions observed between 2000 and 2010 with air mass transport and precipitation at Zeppelin station, Ny-Ålesund, Svalbard". In: *Atmospheric chemistry and physics* 13, pp. 3643–3660.

Twomey, S. (1974). „Pollution and the planetary albedo". In: *Atmospheric Environment* 8, pp. 1251–1256 (cit. on pp. 2, 3).

Wallace, John M. and Peter V. Hobbs (2006a). „6 - Cloud Microphysics". In: *Atmospheric Science (Second Edition)*. Ed. by John M. Wallace and Peter V. Hobbs. Second Edition. San Diego: Academic Press, pp. 209–269 (cit. on p. 2).

– (2006b). *Atmospheric Science*. Academic Press (cit. on p. 6).

Weitkamp, Claus (2005). *Lidar, Range-Resolved Optical Remote Sensing of the Atmosphere*. Springer (cit. on p. 8).

Wendisch, Manfred, Marlen Brückner, J. P. Burrows, et al. (2017). „Understanding Causes and Effects of Rapid Warming in the Arctic“. In: *EOS* 98 (cit. on p. 2).

Willis, Megan D., Heiko Bozem, Daniel Kunkel, et al. (2019). „Aircraft-based measurements of High Arctic springtime aerosol show evidence for vertically varying sources, transport and composition“. In: *Atmospheric chemistry and physics* 19, pp. 57–76.

Wise, Matthew E., Trudi A. Semeniuk, Roelof Bruintjes, et al. (2007). „Hygroscopic behavior of NaCl-bearing natural aerosol particles using environmental transmission electron microscopy“. In: *Journal of geophysical research: Atmospheres* 112 (cit. on p. 6).

Zieger, P., R. Fierz-Schmidhauser, M. Gysel, et al. (2010). „Effects of relative humidity on aerosol light scattering in the Arctic“. In: *Atmospheric Chemistry and Physics* 10, pp. 3875–3890.

Appendix

Appendix 1: Relative frequencies of optical properties for January to April

Tab. 5.1: Relative frequencies of β (532 nm) from January to April for 4 height intervals. H1 = 700-1500 m; H2 = 1500-3000 m; H3 = 3000-5000 m; H4= 5000-10000 m

Beta classes	**H1**	**H2**	**H3**	**H4**
1E-09	0.01	0.01	0.02	0.05
5E-08	0.42	0.61	4.48	45.54
1E-07	0.68	4.95	41.01	27.96
1.5E-07	1.34	15.52	30.12	3.02
2E-07	4.78	23.65	11.20	1.04
2.5E-07	11.43	20.41	3.47	0.45
3E-07	15.47	14.43	1.37	0.19
3.5E-07	16.85	7.63	0.70	0.10
4E-07	12.12	2.95	0.61	0.07
4.5E-07	7.29	1.07	0.35	0.06
5E-07	4.48	0.68	0.29	0.04
5.5E-07	3.30	0.50	0.17	0.02
6E-07	2.64	0.25	0.14	0.01
7E-07	2.98	0.30	0.19	0.02
8E-07	1.97	0.12	0.11	0.01
9E-07	1.20	0.02	0.07	0.01
1E-06	0.61	0.01	0.05	0.01
1.2E-06	0.33	0.02	0.06	0.01
sum	87.90	93.14	94.40	78.62

Tab. 5.2: Relative frequencies of the color ratio (355 / 532 nm) for the four height intervals H1 to H4. In the graphs, H3 and H4 have been left out, since too small percentages of the used data were valid and the relative frequencies were too low to interprete the data.

CR classes	H1	H2	H3	H4
2.0001	0.01	0.00	0.00	0.00
2.2	6.29	2.74	0.53	2.92
2.4	9.28	2.93	0.46	3.06
2.6	10.91	3.37	0.49	3.20
2.8	10.41	4.91	0.54	3.09
3	9.21	5.57	0.66	3.11
3.2	9.46	6.47	0.63	3.12
3.4	6.58	6.67	0.76	3.08
3.6	6.41	6.23	0.88	3.07
3.8	5.31	6.43	1.11	3.04
4	3.65	6.41	1.60	3.01
4.5	4.71	12.18	5.42	7.05
5	2.09	9.42	7.87	6.39
sum	84.32	73.33	20.97	44.12

Tab. 5.3: Relative frequencies of δ (532 nm) from January to April for 4 height intervals. H1 = 700-1500 m; H2 = 1500-3000 m; H3 = 3000-5000 m; H4= 5000-10000 m

Depol classes	H1	H2	H3	H4
0.001	0.84	0.17	0.54	1.44
0.01	30.63	16.47	14.67	13.74
0.015	33.71	36.15	33.22	25.92
0.02	11.86	23.90	22.75	17.97
0.025	5.29	7.35	9.72	8.21
0.03	1.49	2.71	4.51	4.04
0.035	0.62	1.52	1.80	2.28
0.04	0.23	0.56	0.96	1.32
0.05	0.33	0.70	1.29	1.34
0.06	0.29	0.45	0.95	0.68
0.07	0.24	0.34	0.77	0.42
0.12	0.14	0.34	0.44	0.16
sum	85.66	90.65	91.62	77.52

Tab. 5.4: Relative frequencies of the LR from January to April for 4 height intervals. H1 = 700-1500 m; H2 = 1500-3000 m; H3 = 3000-5000 m; H4= 5000-10000 m

LR classes	H1	H2	H3	H4
0.01	0.02	0.02	0.01	0.11
10	22.71	19.16	13.86	2.94
20	18.81	32.46	22.87	3.28
30	15.14	22.61	19.77	3.54
40	7.26	7.50	11.80	3.54
50	1.90	2.36	6.41	3.51
60	0.70	0.77	3.50	3.12
70	0.35	0.23	1.72	2.67
80	0.26	0.09	0.95	2.22
90	0.12	0.03	0.59	1.83
100	0.10	0.01	0.38	1.54
sum	67.37	85.24	81.85	28.28

Appendix 2: Relative frequencies of the aerosol backscatter per height

Tab. 5.5: Relative frequencies of β (532 nm) between 700 - 1500 m for January to April.

Beta classes	January	February	March	April
1E-09	0.00	0.00	0.05	0.00
5E-08	0.01	0.04	1.74	0.16
1E-07	0.07	0.29	2.34	0.60
1.5E-07	0.44	1.00	3.67	0.82
2E-07	2.33	6.75	7.32	4.20
2.5E-07	13.01	9.68	10.94	10.55
3E-07	16.61	16.22	14.07	11.92
3.5E-07	14.48	23.06	14.58	15.52
4E-07	12.75	9.20	15.49	9.64
4.5E-07	7.74	6.64	8.52	4.42
5E-07	4.72	4.72	3.84	4.23
5.5E-07	3.41	4.85	1.34	3.10
6E-07	2.77	4.88	0.31	1.43
7E-07	3.79	4.48	0.24	1.79
8E-07	2.06	3.29	0.10	2.34
9E-07	1.72	1.02	0.06	2.03
1E-06	1.25	0.04	0.04	0.69
1.2E-06	0.58	0.08	0.02	0.60
sum	87.74	96.25	84.67	74.07

Tab. 5.6: Relative frequencies of β (532 nm) between 1500 - 3000 m for January to April.

Beta classes	January	February	March	April
1E-09	0.00	0.00	0.02	0.02
5E-08	0.27	0.00	1.70	1.15
1E-07	2.46	9.99	4.74	2.58
1.5E-07	18.13	16.46	14.11	5.38
2E-07	23.37	22.20	27.19	20.80
2.5E-07	18.47	23.91	20.53	19.11
3E-07	14.43	14.57	14.14	14.65
3.5E-07	8.58	5.73	7.27	9.45
4E-07	3.51	1.49	1.54	7.60
4.5E-07	0.91	1.08	0.31	3.40
5E-07	0.35	1.48	0.15	1.18
5.5E-07	0.18	1.24	0.10	0.80
6E-07	0.16	0.43	0.10	0.49
7E-07	0.48	0.14	0.08	0.48
8E-07	0.17	0.06	0.06	0.22
9E-07	0.02	0.02	0.02	0.02
1E-06	0.02	0.01	0.00	0.00
1.2E-06	0.03	0.01	0.01	0.02
sum	91.55	98.82	92.06	87.34

Tab. 5.7: Relative frequencies of β (532 nm) between 3000 - 5000 m for January to April.

Beta classes	January	February	March	April
1E-09	0.04	0.00	0.00	0.06
5E-08	6.50	2.76	3.78	2.09
1E-07	44.40	54.28	26.38	24.91
1.5E-07	29.38	26.01	37.68	27.10
2E-07	9.18	10.07	13.16	18.15
2.5E-07	2.63	2.03	4.96	7.36
3E-07	0.82	0.32	2.46	3.97
3.5E-07	0.40	0.19	1.14	2.31
4E-07	0.34	0.16	1.31	1.39
4.5E-07	0.19	0.15	0.64	0.84
5E-07	0.19	0.14	0.62	0.37
5.5E-07	0.14	0.08	0.35	0.11
6E-07	0.13	0.05	0.26	0.17
7E-07	0.19	0.08	0.35	0.13
8E-07	0.11	0.03	0.22	0.05
9E-07	0.07	0.01	0.16	0.02
1E-06	0.07	0.02	0.07	0.01
1.2E-06	0.07	0.02	0.10	0.01
sum	94.83	96.43	93.63	89.05

Tab. 5.8: Relative frequencies of β (532 nm) between 5000 - 10000 m for January to April.

Beta classes	January	February	March	April
1E-09	0.07	0.05	0.01	0.09
5E-08	47.03	56.29	35.19	34.36
1E-07	24.53	24.60	36.13	32.76
1.5E-07	2.07	1.00	5.56	6.61
2E-07	1.00	0.34	1.42	2.18
2.5E-07	0.36	0.22	0.56	1.13
3E-07	0.19	0.10	0.15	0.55
3.5E-07	0.10	0.03	0.09	0.31
4E-07	0.06	0.03	0.09	0.21
4.5E-07	0.05	0.02	0.08	0.12
5E-07	0.04	0.01	0.06	0.08
5.5E-07	0.02	0.01	0.01	0.03
6E-07	0.02	0.00	0.02	0.02
7E-07	0.02	0.01	0.02	0.05
8E-07	0.02	0.00	0.01	0.02
9E-07	0.02	0.00	0.02	0.01
1E-06	0.01	0.01	0.01	0.02
1.2E-06	0.02	0.00	0.02	0.02
sum	75.62	82.71	79.46	78.58

Appendix 3: Relative frequencies of the depolarisation ratio per height.

Tab. 5.9: Relative frequencies of δ (532 nm) between 700 - 1500 m for January to April.

Depol classes	January	February	March	April
0.001	0.86	0.63	1.14	0.63
0.01	27.37	34.25	34.47	26.21
0.015	34.46	43.88	23.49	26.79
0.02	10.36	12.54	13.08	13.57
0.025	6.47	3.53	5.65	4.20
0.03	2.23	1.01	0.93	0.88
0.035	0.78	0.34	0.42	1.13
0.04	0.29	0.04	0.25	0.47
0.05	0.46	0.04	0.53	0.08
0.06	0.47	0.01	0.36	0.08
0.07	0.42	0.04	0.17	0.11
sum	84.16	96.32	80.51	74.15

Tab. 5.10: Relative frequencies of δ (532 nm) between 1500 - 3000 m for January to April.

Depol classes	January	February	March	April
0.001	0.11	0.36	0.00	0.34
0.01	21.19	18.30	8.15	10.52
0.015	34.45	43.53	32.93	31.12
0.02	19.03	30.11	26.52	22.18
0.025	4.87	4.86	12.07	13.66
0.03	3.12	1.16	2.92	4.57
0.035	2.21	0.46	1.15	2.23
0.04	0.82	0.06	0.63	0.66
0.05	0.97	0.00	0.81	1.12
0.06	0.71	0.00	0.51	0.46
0.07	0.27	0.00	0.96	0.08
sum	87.75	98.83	86.65	86.95

Tab. 5.11: Relative frequencies of δ (532 nm) between 3000 - 5000 m for January to April.

Depol classes	January	February	March	April
0.001	0.01	0.96	0.05	2.76
0.01	17.96	14.81	11.41	7.88
0.015	28.92	50.06	26.73	21.64
0.02	21.61	21.62	26.19	22.85
0.025	8.97	5.63	11.66	19.16
0.03	4.43	1.55	5.99	9.27
0.035	1.72	0.72	2.72	2.96
0.04	1.25	0.37	1.19	0.82
0.05	2.00	0.48	1.28	0.41
0.06	1.43	0.15	1.33	0.20
0.07	0.97	0.09	1.41	0.28
sum	89.26	96.43	89.94	88.21

Tab. 5.12: Relative frequencies of δ (532 nm) between 5000 - 10000 m for January to April.

Depol classes	January	February	March	April
0.001	0.74	1.69	1.61	3.32
0.01	11.92	21.81	10.29	7.93
0.015	28.90	30.69	21.26	11.49
0.02	18.19	14.71	22.82	14.82
0.025	6.81	5.78	11.91	12.09
0.03	2.87	3.00	5.15	9.18
0.035	1.40	2.09	2.48	5.99
0.04	0.81	1.17	1.15	4.14
0.05	0.84	0.95	1.02	5.17
0.06	0.58	0.35	0.46	2.41
0.07	0.47	0.15	0.41	0.94
sum	73.54	82.38	78.56	77.48

Appendix 4: Relative frequencies of the color ratio per height

Tab. 5.13: Relative frequencies of the color ratio (355 / 532 nm) for 700 - 1500 m for January to April.

CR classes	January	February	March	April
2.0001	0.01	0.00	0.00	0.03
2.2	8.67	4.66	4.18	5.33
2.4	9.59	11.00	7.37	7.75
2.6	7.06	16.54	13.62	6.24
2.8	7.55	16.20	10.33	7.34
3	8.52	10.59	9.49	7.83
3.2	10.92	9.10	7.38	8.96
3.4	7.84	5.72	5.12	6.87
3.6	8.16	4.82	5.20	5.99
3.8	7.18	4.54	3.52	3.54
4	4.67	3.07	2.84	2.66
4.5	4.27	5.46	4.18	5.77
5	1.52	2.14	2.86	2.64
sum	85.98	93.84	76.08	70.93

Tab. 5.14: Relative frequencies of the color ratio (355 / 532 nm) for 1500 - 3000 m for January to April.

CR classes	January	February	March	April
2.0001	0.00	0.00	0.00	0.00
2.2	5.13	0.54	1.13	2.15
2.4	3.81	2.51	2.06	2.28
2.6	3.54	2.83	3.70	3.35
2.8	4.12	5.37	5.72	5.18
3	4.75	5.94	6.69	5.55
3.2	5.78	5.71	8.04	7.88
3.4	5.76	6.29	8.15	8.12
3.6	5.87	6.68	6.08	6.86
3.8	7.12	6.22	5.56	6.02
4	7.30	7.05	4.44	5.42
4.5	13.42	12.51	9.35	12.38
5	9.87	9.66	8.97	7.92
sum	76.48	71.33	69.89	73.12

Tab. 5.15: Relative frequencies of the color ratio (355 / 532 nm) for 3000 - 5000 m for January to April.

CR classes	January	February	March	April
2.0001	0.00	0.00	0.00	0.00
2.2	0.59	0.25	0.63	0.84
2.4	0.45	0.21	0.62	0.77
2.6	0.55	0.26	0.51	0.83
2.8	0.74	0.19	0.46	0.78
3	0.87	0.26	0.61	0.94
3.2	0.78	0.24	0.70	0.91
3.4	0.97	0.21	0.68	1.50
3.6	0.94	0.30	0.94	2.01
3.8	1.30	0.37	1.17	2.17
4	1.84	0.49	1.94	2.70
4.5	5.12	2.98	7.77	7.85
5	6.51	5.82	11.86	10.05
sum	20.65	11.58	27.90	31.34

Tab. 5.16: Relative frequencies of the color ratio (355 / 532 nm) for 5000 - 10000 m for January to April.

CR classes	January	February	March	April
2.0001	0.00	0.00	0.00	0.00
2.2	2.89	2.40	3.46	3.27
2.4	3.00	2.44	3.72	3.39
2.6	2.97	2.75	3.95	3.73
2.8	2.78	2.68	3.89	3.63
3	2.85	2.61	3.79	4.03
3.2	2.80	2.70	3.66	4.30
3.4	2.74	2.83	3.57	4.12
3.6	2.70	2.88	3.56	3.96
3.8	2.67	2.96	3.47	3.77
4	2.72	2.85	3.46	3.59
4.5	6.27	6.89	8.30	7.90
5	5.80	6.63	7.21	6.37
sum	40.20	40.60	52.03	52.06

Appendix 5: Relative frequencies of the Lidar ratio per height

Tab. 5.17: Relative frequencies of the Lidar ratio for 700 - 1500 m for January to April.

LR	January	February	March	April
0.01	0.03	0.00	0.02	0.00
10	36.85	10.13	15.24	13.35
20	19.79	21.49	18.09	9.40
30	6.28	35.29	8.92	13.27
40	2.50	14.96	3.41	15.47
50	1.03	1.47	2.03	6.29
60	0.17	0.22	1.79	1.79
70	0.00	0.03	1.07	1.02
80	0.00	0.00	0.51	1.46
90	0.00	0.00	0.04	1.10
100	0.00	0.00	0.02	0.96
sum	66.65	83.60	51.14	64.09

Tab. 5.18: Relative frequencies of the Lidar ratio for 1500 - 3000 m for January to April.

LR classes	January	February	March	April
0.01	0.01	0.01	0.03	0.00
10	18.55	15.93	27.15	12.42
20	36.13	32.46	30.07	22.54
30	22.26	29.80	14.88	22.49
40	5.57	11.10	5.22	11.17
50	1.61	3.20	1.40	5.45
60	0.53	0.85	0.27	2.62
70	0.17	0.17	0.10	0.98
80	0.05	0.08	0.03	0.40
90	0.01	0.01	0.03	0.12
100	0.00	0.01	0.01	0.06
sum	84.88	93.63	79.22	78.25

Tab. 5.19: Relative frequencies of the Lidar ratio for 3000-5000 m for January to April.

LR classes	January	February	March	April
0.01	0.00	0.00	0.01	0.01
10	15.39	13.00	14.44	8.48
20	26.44	24.38	20.27	9.93
30	21.41	23.71	17.06	8.75
40	11.72	14.49	11.15	6.54
50	6.17	7.17	6.55	5.11
60	3.28	3.76	3.52	3.74
70	1.53	1.76	1.73	2.39
80	0.67	0.97	1.00	1.95
90	0.39	0.40	0.73	1.56
100	0.21	0.16	0.46	1.46
sum	87.20	89.80	76.90	49.93

Tab. 5.20: Relative frequencies of the Lidar ratio for 5000-10000 m for January to April.

LR classes	January	February	March	April
0.01	0.00	0.00	0.12	0.82
10	3.50	3.05	2.38	1.59
20	3.97	3.68	2.78	0.45
30	4.38	4.13	2.70	0.44
40	4.25	4.27	2.74	0.47
50	4.20	4.13	2.86	0.47
60	3.73	3.72	2.50	0.35
70	3.11	3.23	2.23	0.37
80	2.56	2.76	1.77	0.37
90	2.07	2.21	1.53	0.50
100	1.63	1.91	1.39	0.50
sum	33.41	33.07	22.99	6.32

List of Figures

List of Tables